Pixel-level parameter optimization of a terrestrial biosphere model for improving estimation of carbon fluxes with an efficient model–data fusion method and satellite-derived LAI and GPP data

Rui Ma[1], Jingfeng Xiao[2], Shunlin Liang[3], Han Ma[3], Tao He[1], Da Guo[4], Xiaobang Liu[1], and Haibo Lu[5]

[1]School of Remote Sensing and Information Engineering, Wuhan University, Wuhan 430079, China
[2]Earth Systems Research Center, Institute for the Study of Earth, Oceans, and Space, University of New Hampshire, Durham, NH 03824, USA
[3]Department of Geography, University of Hong Kong, Hong Kong SAR 999077, China
[4]College of Resources and Environment, University of Chinese Academy of Sciences, Beijing 100049, China
[5]School of Atmospheric Sciences, Sun Yat-sen University, Zhuhai 519082, China

Correspondence: Rui Ma (marui6922@whu.edu.cn) and Shunlin Liang (shunlin@hku.hk)

Abstract. Inaccurate parameter estimation is a significant source of uncertainty in complex terrestrial biosphere models. Model parameters may have large spatial variability, even within a vegetation type. Model uncertainty from parameters can be significantly reduced by model–data fusion (MDF), which, however, is difficult to implement over a large region with traditional methods due to the high computational cost. This study proposed a hybrid modeling approach that couples a terrestrial biosphere model with a data-driven machine learning method, which is able to consider both satellite information and the physical mechanisms. We developed a two-step framework to estimate the essential parameters of the revised Integrated Biosphere Simulator (IBIS) pixel by pixel using the satellite-derived leaf area index (LAI) and gross primary productivity (GPP) products as "true values." The first step was to estimate the optimal parameters for each sample using a modified adaptive surrogate modeling algorithm (MASM). We applied the Gaussian process regression algorithm (GPR) as a surrogate model to learn the relationship between model parameters and errors. In our second step, we built an extreme gradient boosting (XGBoost) model between the optimized parameters and local environmental variables. The trained XGBoost model was then used to predict optimal parameters spatially across the deciduous forests in the eastern United States. The results showed that the parameters were highly variable spatially and quite different from the default values over forests, and the simulation errors of the GPP and LAI could be markedly reduced with the optimized parameters. The effectiveness of the optimized model in estimating GPP, ecosystem respiration (ER), and net ecosystem exchange (NEE) were also tested through site validation. The optimized model reduced the root mean square error (RMSE) from 7.03 to 6.22 $\mathrm{gC\,m^{-2}}$ per 8 d for GPP, 2.65 to 2.11 $\mathrm{gC\,m^{-2}}$ per 8 d for ER, and 4.45 to 4.38 $\mathrm{gC\,m^{-2}}$ per 8 d for NEE. The mean annual GPP, ER, and NEE of the region from 2000 to 2019 were 5.79, 4.60, and $-1.19\,\mathrm{Pg\,yr^{-1}}$, respectively. The strategy used in this study requires only a few hundred model runs to calibrate regional parameters and is readily applicable to other complex terrestrial biosphere models with different spatial resolutions. Our study also emphasizes the necessity of pixel-level parameter calibration and the value of remote sensing products for per-pixel parameter optimization.

1 Introduction

Accurate quantification of the terrestrial carbon budget is crucial for understanding the global carbon cycle and biosphere–atmosphere interactions, and informing climate projections (Fernández-Martínez et al., 2018; Piao et al., 2020). Land surface models (LSMs) built on process-based mechanisms of atmosphere–biosphere interactions are often

used to simulate the behavior of the terrestrial carbon cycle in response to a changing climate (Peaucelle et al., 2019). These models typically use a large number of parameters. Prescribed values of model parameters based on a theoretical assumption, empirical analysis, or field measurements are prone to substantial uncertainties which can engender inaccurate projections in modeling (Barman et al., 2014; Keenan et al., 2012; Kuppel et al., 2014). Parameter estimation is becoming more challenging, especially when greater details are introduced to enhance the authenticity and interpretability of LSMs (Famiglietti et al., 2021).

Model–data fusion (MDF) is an increasingly used method that can be leveraged to reduce the model–data misfit by calibrating parameters. Researchers have mainly used the site and sample measurements, raw reflectivity observations, and satellite-based products to estimate parameters in complex terrestrial biosphere models, and significant progress has been made in the integration of univariate observations (MacBean et al., 2016). However, due to the complex relationship between model variables, univariate assimilation is often not enough to constrain the vegetation parameters involved in multiple surface processes, and it is still necessary to introduce other data streams to increase the constraints on model parameters (Fernández-Martínez et al., 2018; Liu et al., 2015; Schürmann et al., 2016; Zobitz et al., 2014). For example, soil moisture observations can be regarded as an additional constraint of a plant functional type (PFT) due to the tight coupling of carbon and water cycles in vegetation photosynthesis (Scholze et al., 2016), and some remote sensing products, such as the fraction of photosynthetically active radiation data (FAPAR) and leaf area index (LAI) could bring phenology information in constraining long-term vegetation dynamics. Joint constraints of LAI or FAPAR products and in situ observations of carbon fluxes or atmospheric CO_2 concentration have already been explored in reducing parameters uncertainties (Forkel et al., 2014; Bacour et al., 2015). Although remote sensing has provided high-precision products, there are only a limited number of variables available. Using remote sensing products as a reference to calibrate the parameters of the surface model can not only improve the simulation accuracy of target variables but also affect related processes in the model, which thereby can improve the simulation accuracy of other related variables (e.g., carbon storage, respiration), and our understanding of terrestrial ecosystem processes and their interactions with the environment.

The parameter estimation of complex models has been well studied at the site scale. Many researchers used observations to optimize parameters at the site scale and then applied the optimized parameters to regions. However, when a PFT covers a broad area, ecosystem characteristics, density, or disturbance history can vary substantially across the region. In this case, site-scale parameters with a small footprint cannot be considered spatially representative, and the relationship between observations and models may not be spatially scalable (Raoult et al., 2016; Xiao et al., 2014; Zhou et

al., 2020). Finding a globally applicable parameter scheme is complicated for LSMs, as it requires a high computational cost (Gong and Duan, 2017). Machine learning (ML) approaches are flexible in adapting to an increasing stream of geospatial products, making it easy to extract patterns and combine them with physical models as an additional source of information. It offers an opportunity to improve or accelerate parameterizations by integrating model simulation and multiple observations or high-quality spatial products more intensively in different ways. For example, Chaney et al. (2016) carried out parameter calibration at 85 eddy covariance flux sites, and then obtained the spatial parameters using extra trees and combining local environmental characteristics. Although the parameters showed significant spatial variability, their study did not verify the performance of the optimized model. Tao et al. (2020) constrained parameters at the site scale to improve the soil organic carbon simulation and then extended the optimized parameters to the United States, utilizing a neural network. Their results showed that the model error was significantly reduced when the spatial heterogeneity of optimal parameters was considered. These studies using flux sites to calibrate parameters can ensure the parameter accuracy at each site, while it is likely to cause potential problems of overfitting due to limited training samples, which makes it difficult to guarantee the accuracy when extending the resulting optimal parameters to a broad region using ML.

To date, few researchers conducted pixel-level parameterization because parameter optimization often depends on a large number of parameter samplings and model operations, especially when using the Markov chain Monte Carlo (MCMC) method as the optimization algorithm. MCMC is usually applied to model parameter calibration to obtain the optimal posterior probability distribution of parameters (Yuan et al., 2012; Safta et al., 2015). It typically requires thousands of model simulations, which are excessively expensive for complex LSMs that may take hours for each model simulation (Fer et al., 2018). ML can be an innovative method to conduct surrogate modeling or emulation in parameter optimization (J. Li et al., 2018; Reichstein et al., 2019). ML is regarded as an effective method to speed up model parameterizations and can make better use of the abundant spatial information provided by the multisource high-precision remote sensing products. Researchers have proved the feasibility of surrogate modeling and indicated that once the ML emulator is trained well, the optimization speed can be increased by an order of magnitude without much loss of accuracy (Sawada and Koike, 2014; Fer et al., 2018). For example, Gong and Duan (2017) pointed out that using a surrogate model can reduce the number of model runs from 10^6 to a few hundred or thousands with acceptable accuracy. The integration of physical and ML models may not only achieve improved performance but may also significantly improve computing speed, and the optimization of model parameters using multisource observations based

on surrogate modeling has the potential for improving the accuracy of regional or global LSMs (Zhang et al., 2019; Xu et al., 2018).

Some researchers considered finding unknown regional parameters using an ML emulator but with a very coarse resolution (Dagon et al., 2020; J. Li et al., 2018). This is because a large number of model runs are still needed to train the surrogate model to ensure its accuracy, even though adaptive surrogate modeling-based optimization algorithms have been developed to reduce the initial training samples (J. Li et al., 2018; Gong and Duan, 2017). In this paper, we explored a two-step method of combining ML and a physical model to improve the calibration speed of spatial parameters, made full use of high-quality remote sensing products to calibrate the model at each pixel, and carried out a study on the deciduous forests (DF) in the eastern United States. We first performed pixel-level parameter calibration using surrogate running instead of a terrestrial model within samples in our region, and then expanded the optimal parameters obtained from samples into spatial distribution using the ML approach with several environmental variables. In this way, the results of our first step can provide more samples for training ML model than directly using ML for spatial expansion of optimized parameters. Compared to studies that simply use surrogate models to optimize parameters, our second-step ML extension makes it easier to obtain large-scale, high-resolution parameter space distributions.

This paper is organized as follows. Section 2 briefly introduces a terrestrial model and related data sources. Section 3 describes the two-step pixel-by-pixel region parametrization algorithm and the experimental setting. Section 4 shows the results of thus optimizing parameters and presents a spatial analysis of carbon fluxes before and after the optimization. Uncertainty analysis and future work are described in Sect. 5, followed by a conclusion in Sect. 6.

2 Models and data

2.1 Model framework and running strategy

2.1.1 Model description

The Integrated Biosphere Simulator (IBIS) model integrates many land-surface ecosystem processes into a complex physical mechanism model, which is divided into the land surface, vegetation phenology, carbon balance, and vegetation dynamic modules (Foley et al., 1996; Yuan et al., 2014). It has a hierarchical structure operating on 60 min or 1-year time steps. IBIS considers three snow layers and six soil layers in each pixel and determines PFTs based on different ecological characteristics. Detailed information about IBIS is available in Foley et al. (1996) and Kucharik et al. (2000).

A simple function is used in IBIS to describe the relationship between leaf behaviors and phenological status, which forecasts the onset of budburst when suitable temperatures are reached. It describes the defoliation when the 10 d average daily air temperature is below 5 °C in autumn. The potential LAI (pLAI), also known as the yearly maximum leaf area, is calculated for the growing season based on the leaf carbon biomass of previous years, as shown in Eq. (1). When simplified phenology (phen, shown below and calculated by the accumulated growing degree day and several temperature parameters) is considered for pLAI, the overall growth dynamics of vegetation leaves can be obtained for each year (Cao et al., 2015):

$$pLAI = leaf\ biomass \times specla, \tag{1}$$

$$LAI = pLAI \times phen, \tag{2}$$

where specla refers to specific leaf area ($m^2\,kg^{-1}$).

Biomass allocation in the IBIS model is updated annually, and therefore it is difficult to accurately describe the influence of meteorological factors on LAI and to capture the detailed dynamics of leaves (Kucharik et al., 2006). Capturing the daily dynamics of LAI requires changes in the leaf biomass pool each day. For this process, we incorporated part of the carbon allocation in the data assimilation linked ecosystem carbon (DALEC) model (Chuter et al., 2015) into the original IBIS model, a simple box model evaluating daily six-carbon pools for deciduous forests. The photosynthesis rate of deciduous forests conveyed following the Farquhar equation (Farquhar et al., 1980) can be expressed as the minimum of light and Rubisco-limited rates of photosynthesis in the IBIS model, and then we can obtain gross primary productivity (GPP) at each time step on a pixel basis. Photosynthates stored in daily GPP will be allocated to the foliage (C_f), woody (C_w), and root (C_r) pools within a discrete dynamical process as defined in the DALEC model. The dynamic LAI values can be obtained by dividing daily C_f by the leaf mass per area. LAI values most directly limit specific growth or carbon allocation characteristics, potentially influencing the seasonal dynamics of carbon-related fluxes. Net ecosystem exchange (NEE) is defined as the difference between ecosystem respiration (ER) and GPP. In this paper, a positive value of NEE represents carbon release, while a negative value indicates carbon uptake.

2.1.2 Running strategy

We simulated the LAI and carbon fluxes for the deciduous forests in the eastern United States from 2000 to 2019 at a spatial resolution of $0.05° \times 0.05°$. All model simulations were forced with daily climate drivers, CO_2 concentration, and soil properties. We employed fixed vegetation instead of dynamic runs to avoid model errors from building forest species structures while simulating ecological processes. All the datasets used to drive the model are described in Sect. 2.2.

For model initialization, the improved IBIS was cyclically spun up for 50 years by repeating meteorological datasets in 2000. The final soil and carbon states of initialization run

at each pixel reached a quasi-equilibrium and were saved as inputs for the subsequent transient simulation. Default values for the initial carbon pools (six pools for DF) used in DALEC modeling were set to the same scheme as Chuter et al. (2015).

2.2 Data sources

2.2.1 Model forcing

Initial soil and vegetation properties and daily climate data are required in IBIS. The soil parameters include soil sand and clay content (%), which were gathered from available comprehensive, gridded Global Soil Datasets for use in Earth System Models (GSDE) with a resolution of 30 arcsec (Shangguan et al., 2014). Forcing meteorological datasets are maximum and minimum temperature (°C), precipitation (mm), wind speed (m s^{-1}), specific humidity (%), pressure (Pa), and cloud cover (%). All forcing datasets were resampled to match the model resolutions (0.05°) using bilinear resampling, and hourly pressure was aggregated into daily values. The global CO_2 concentration was based on the measurements at the Mauna Loa Observatory, Hawaii started in 2000 (Thoning et al., 1989). Information on all the datasets is summarized in Table 1.

The primary vegetation type in each pixel was identified by the high-resolution land cover maps from the National Land Cover Database (NLCD, 30 m) (Homer et al., 2020, available on http://www.mrlc.gov, last access: 9 January 2021). The NLCD offers a suite of the national land cover of the United States and associates changes that were upscaled to the model running resolution based on the majority land cover type (>50 %) method in resampling. We extracted data on deciduous broad-leaved forests in the eastern United States with the resampled land cover map.

2.2.2 Assimilated remotely sensed products

This study used global LAI and GPP products from the Global Land Surface Satellite (GLASS) suite as "observations" ("true values") for parameter calibration on a spatial scale. This dataset has long-time coverage, high spatial resolution (500 m and 0.05°), and temporal and spatial continuity. It was found to have high accuracy in a site validation and product comparison test (Liang et al., 2021) and has been widely used in many studies (Chen et al., 2019; Ryu et al., 2018; Kumar et al., 2020). We used the latest version of the GLASS LAI product, which was obtained from the bidirectional long short-term memory deep learning model (Ma and Liang, 2022). According to the validation by ground measurements, the overall accuracy of this product was much improved ($R^2 = 0.73$, RMSE $= 0.82$ m^2 m^{-2}) over the Moderate Resolution Imaging Spectroradiometer (MODIS) LAI product ($R^2 = 0.57$, RMSE $= 1.08$ m^2 m^{-2}) (Ma and Liang, 2022). The GLASS GPP product with 0.05° spatial resolution was derived from a revised light-use efficiency model

Table 1. Description of the datasets used in this study*.

Products		Time spin	Spatial res.	Temporal res.	Variables	Reference
Category 1: model forcing (model inputs)						
Climate	Daily Surface Weather Data (Daymet)	2000–2019	1 km	daily	tmin, tmax, prec	Thornton et al. (2021)
	Gridded Surface Meteorological dataset (gridMET)	2000–2019	2.5'	daily	vs, sph,	Abatzoglou (2013)
	The North American Land Data Assimilation System project (NLDAS-2)	2000–2019	0.125°	hourly	pa	Land Data Assimilation Systems (LDAS, 2016)
	North American Regional Reanalysis data (NARR)	2000–2019	32 km	daily	cld	the National Centers for Environmental Prediction (NCEP, 2005)
Auxiliary	CO_2 concentration	2000–2019	–	yearly	CO_2	Thoning et al. (1989)
	GSDE	–	30″	–	soil sand, soil clay	Shangguan et al. (2014)
	NLCD	2001	30 m	yearly	land cover	Homer et al. (2020)
Category 2: ground observations (NEE validation)						
	FluxNet2015	site	site	daily	NEE	Pastorello et al. (2020)
	AmeriFlux	site	site	daily	NEE	–
Category 3: satellite products (MDF and validation)						
	GLASS LAI	2000–2015	0.05°	8 d	LAI	Ma and Liang (2022)
	GLASS GPP	2000–2017	0.05°	8 d	GPP	Zheng et al (2020)

* Abbreviations: res: resolution; tmax: the maximum air temperature (°C); tmin: the minimum air temperature (°C); prec: precipitation (mm); vs: wind speed (m s^{-1}); sph: specific humidity (%); pa: pressure (Pa); cld: cloud fraction (%).

(EC-LUE model), which had a better performance at most sites ($R^2 = 0.81$, RMSE $= 2.13\,\mathrm{gC\,m^{-2}\,d^{-1}}$) than FLUX-COM and several process-based biophysical models (Zheng et al., 2020).

2.2.3 Flux observations

We collected 14 eddy covariance flux sites of deciduous forests in the eastern United States from FLUXNET2015 ("Tier 1") (Pastorello et al., 2020, https://fluxnet.org/data/fluxnet2015-dataset/, last access: 11 June 2020) and Amer-iFlux network (http://public.ornl.gov/ameriflux, last access: 26 June 2020) (Table S1). Half-hourly or hourly measurements from AmeriFlux datasets were aggregated into different temporal scales. Daily values were indicated as invalid if more than 20 % of the data were missing on a given day. Site data from FLUXNET2015 were filtered considering quality information flags provided by the FULLSET data product (NEE_VUT_REF_QC ≥ 0.5) (Yuan et al., 2012).

3 Model–data fusion for pixel-level parameterization

3.1 Modified adaptive surrogate modeling (MASM)

We employed adaptive surrogate modeling in this study to establish a fast and practical framework for the iterative optimization of a complex physical model. We slightly improved the adaptive surrogate modeling-based optimization parameter optimization and distribution estimation (ASMO–PODE) method proposed by Gong and Duan (2017). We applied Bayesian optimization twice to reduce the time cost of Monte Carlo iterations. The modified procedure (Fig. S1) is as follows.

- *Step 1. Initial random sampling.* We generated points in a uniformly distributed parameter space by randomly sampling using the good lattice point approach with ranked Gram–Schmidt decorrelation (Owen, 1994). As Wang et al. (2014) pointed out, the ASMO method performs better when the number of initial points is set to 15–20 times the number of the parameters; we chose 18 as our initial sampling multiple. With the sampled points, the dynamic model (IBIS) was run to obtain the corresponding target variables (daily LAI and GPP, as y_t^M in Eq. 3).

$$y_t^M = f_M(x_t, \theta, \mathrm{ini}) + R, \qquad (3)$$

where y_t^M is the modeled target variables (e.g., LAI, GPP) at time t, f_M is the IBIS model, x_t represents the forcing datasets (Table 1), θ represents the parameters, ini represents the initial soil and carbon pools after spinning up, and R represents the model errors.

- *Step 2. Cost function (CF) and surrogate model construction.* We used the GLASS products (see

Sect. 2.2.2) as the "observations" (i.e., "true values") to implement pixel-level parameter schemes to calibrate the model parameters. Under the observation constraints, the posterior probability distribution of parameters can be obtained with Bayes' rules and is proportional to the likelihood and prior probability density: TS2

$$P\left(\theta_i | y_t^O\right) \propto P\left(y_t^O | \theta_i\right) P(\theta) = L\left(\theta_i | y_t^O\right) P(\theta_i)$$
$$\theta \sim \mathrm{uniform\ (range)};\ i = 1, 2, 3, \ldots, n, \quad (4)$$

where y_t^O is the observation, $P(\theta_i | y)$ denotes the posterior probability density functions of selected parameters given by the y, $P(y|\theta_i)$ means likelihood, $P(\theta_i)$ $(i = 1, 2, 3, \ldots, n)$ represents prior distribution (set as uniform), and n is the number of sensitive parameters. The distribution bounds of each parameter are shown in Table 2. We aggregated the daily variables simulated by the model into 8 d and constructed the CF with observations.

$$L\left(\theta_i | y_t^O\right) = (2\pi\sigma)^{-n/2} \prod_t \exp\left\{-\frac{[y_t^O - y_t^M]^2}{2\sigma^2}\right\}, \quad (5)$$

where σ^2 is the error variance of each observation. We assumed that the errors between the model and the observation $(y_t^O - y_t^M)$ are independent (i.e., the covariance is zero), and therefore σ^2 here is expressed by the variance of each observation product (Yuan et al., 2012). We used $-2\log(L)$ as our final target function.

$$\mathrm{CF}_t^s = f_s(\mathrm{CF}_t^M, \theta_{\mathrm{sam}}), \qquad (6)$$

where CF_t^s stands for CF estimated from the GPR (Gaussian process regression algorithm model) (f_s), CF_t^M stands for CF estimated from IBIS model (f_M), and θ_{sam} denotes sampled parameters.

- *Step 3. Surrogate optimization protocol based on the MASM algorithm.* We performed global optimization on the GPR model using MASM, which requires many iterative operations that cost much less than running the highly complex IBIS model directly. One slight difference between MASM and the ASMO–PODE is that we applied two Bayesian optimizations for the GPR model. The first one (Fig. S1, Bayes1) was mainly the same as Gong's method (Gong and Duan, 2017), but we reduced the number of Monte Carlo iterations and set it to 10 000 to establish a relatively high-precision GPR model. The second application (Fig. S1, Bayes2) was aimed mainly at the repeated iteration of the GPR model obtained in the previous step. After running Bayes1, we calculated the error between the CF estimated by the GPR model (CF_t^s) and the original model (CF_t^M), as shown

by Eq. (7).

$$\text{RMSE} = \sqrt{\frac{1}{n}\sum_{n=0}^{n}(\text{CF}_t^s - \text{CF}_t^M)^2} \qquad (7)$$

$$\text{GR} = \sqrt{\frac{N_2 - 1}{N_2} + \frac{N_{\text{chain}} + 1}{N_{\text{chain}} \times N_2} \times \frac{B}{W}}, \qquad (8)$$

where B represents the variance between the averaged
values of each chain and W is the average of the variances within each chain.

At the end of each Monte Carlo iteration in Bayes1, five
representative samples were selected adaptively from the
posterior distribution of parameters and were then used as
inputs to the IBIS model to obtain the corresponding CF_t^M.
A new sample scheme containing those representative points
was used to update the GPR model again. This procedure significantly reduced the running time of the initial model and
obtained a relatively high-precision surrogate model when
the first stop criterion was reached (Niter $= 200$). In the second optimization (Bayes2), we repeated the iterative optimization of the finally established GPR model and added the
Gelman and Rubin (GR) factor shown in Eq. (8) as the index
to judge the convergence of the Markov chain. When the GR
factor was less than 1.2, the Markov chain was considered to
have converged, and the result was considered credible and
repeatable (Gelman and Rubin, 1992). The model was run
for both initial sampling (Fig. S1, Run1) and adaptive resampling (Fig. S1, Run2), and the total number of model evaluations was Npars $\times 18 + 5 \times$ Niter. The model was run in
parallel using MATLAB. Compared with the parameter calibration for the original model, this number was reduced by
an order of magnitude, which greatly reduced the computational resources.

3.2 Experimental design for generating pixel-level parameter estimates

3.2.1 Parameter screening

Adding a new module inevitably introduces more parameters
(Sect. 2.1.1), resulting in higher computational costs. Before
calibration, we needed to screen parameters and select the
ones with the most influence on the target variables for calibration. A few parameters related to photosynthesis, carbon
allocation, respiration, and water stress were considered in
our revised IBIS model. All the parameters were restricted
to a predefined range according to several published studies (Cunha et al, 2013; Varejão et al., 2013; Bloom et al.,
2016; Chuter et al., 2015; Lu et al., 2017). Table 2 lists all
parameters, together with the prior ranges and their descriptions. Some parameters are independent of vegetation types
by default (e.g., alpha3 and theta3), while those related to
turnover time or allocation are generally regarded to vary by

type of vegetation (e.g., tauleaf, aleaf, and aroot). We randomly chose 1/10 of the deciduous forest pixels (~ 4200 pixels) and then adopted the Morris approach (Morris, 1991) to
roughly remove parameters with low influence on our target
variables (LAI and GPP) (Fig. 1). We finally determined 10
sensitive parameters, including seven LAI-sensitive parameters (vmax, p5, p14, p15, p17, p18, and p20) and seven GPP-
sensitive parameters (alpha3, theta3, beta3, vmax, p5, p14,
and p20) for further calibration.

3.2.2 Model–data fusion on samples

We randomly selected another sample (~ 4200 pixels) in the
deciduous forest ranges of the eastern United States. The
model was run for 20 years between 2000 and 2019, with
2000 used as the spin-up year and 2001–2009 as the calibration period. The observed and simulated values of the remaining time (years after 2009) were used for independent
verification.

A pixel-by-pixel optimization was performed stepwise for
each sample using the MASM method with the GPP and LAI
from the GLASS products as the observed values. The daily
GPP simulated by the model was aggregated into 8 d, and
the MASM method was used for iterative optimization to
obtain the posterior probability distribution of sensitive parameters of GPP. Considering p5, p14, and p20 have more
obvious effects on LAI (Fig. 1), we only used mean values
of alpha3, theta3, beta3, and vmax as the fixed inputs for
the second step optimization with GLASS LAI as the reference. Adopting such a stepwise optimization required the
use of a "parameter block" approach so that each data stream
could optimize only the more strongly correlated parameters
(Wutzler and Carvalhais, 2014). We tested the effect of optimization order on a small number of samples, and the results
showed no significant differences. A multivariable stepwise
optimization performed by Alton (2013) also showed that optimization order did not distinctly change the results.

3.2.3 Spatial expansion using the XGBoost approach

The optimal parameter scheme of each sample was obtained
after calibration. Considering the spatial differences in the
environmental characteristics, the machine learning (ML)
method was used to expand the optimal scheme of the samples. We used the eXtreme Gradient Boosting (XGBoost)
algorithm to describe the nonlinear relationship between
parameters and environment variables, which has achieved
great success in ML and has been widely used in remote
sensing classification, surface variable inversion, and information extraction (Zhong et al., 2019; Pilaš et al., 2020; Liu
et al., 2021).

Similar to sample running, the regional simulation was
also forced with multisource driving datasets (Table 1) and
adopted the same spin-up scheme to reach equilibrium. We
ran the spatial-scale parameters predicted by XGBoost back

Table 2. Description and prior ranges of IBIS–DALEC parameters.

No.	Parameters	Description	Unit	Default	Min	Max
Parameters for IBIS model						
1	alpha3	intrinsic quantum efficiency for C_3 plants	–	0.06	0.05	0.09
2	theta3	coupling coefficient of C_3 photosynthesis		0.97	0.6	0.996
3	beta3	coupling coefficient of C_3 photosynthesis	–	0.99	0.6	0.996
4	gammaub	intrinsic quantum efficiency for C_3		0.015	0.0075	0.0225
5	coefmub	"m" coefficient for stomatal conductance relationship		10	8	15
6	coefbub	"b" coefficient for stomatal conductance relationship		0.01	0.005	0.015
7	vmax	the maximum carboxylase capacity of Rubisco	$molCO_2\, m^{-2}\, s^{-1}$	3.00×10^{-5}	2.00×10^{-5}	8.00×10^{-5}
8	specla	specific leaf area	$m^2\, kg^{-1}$	12.5	10	20
9	tauleaf	foliar biomass turnover time constant	yr	2	0.05	5
10	tauroot	fine root biomass turnover time constant	yr	1	0.05	1.5
11	tauwood0	stem biomass turnover time constant	yr	50	25	75
12	aleaf	carbon allocation fraction to leaves		0.3	0.15	0.45
13	aroot	carbon allocation fraction to fine roots		0.2	0.05	0.35
14	tempvm	parameter thermal stress Vmax	–	3500	3000	4000
15	rgrowth	growth respiration coefficient	–	0.3	0.1	0.5
16	rroot	maintenance respiration coefficient for root	s^{-1}	1.25	0.625	2.5
17	rwood	maintenance respiration coefficient for wood	s^{-1}	0.0125	0.00625	0.2
18	beta1	parameter related to the distribution of fine root lower	–	0.95	0.75	0.99
19	beta2	parameter related to the distribution of fine root upper	–	0.975	0.75	0.99
20	stressfac	moisture stress factor	–	−5	−6.5	−3.5
Parameters for DALEC module						
21	p2	fraction of GPP respired autotrophically		0.45	0.2	0.7
22	p3	fraction of NPP allocated to foliage		0.4	0.01	0.5
23	p5	turnover rate of foliage	d^{-1}	0.06	1.00×10^{-4}	0.1
24	p10	parameter in temperature sensitivity rate		0.073	0.05	0.2
25	p12	GDD value causing leaf out		240	200	400
26	p13	minimum daily temperature causing leaf fall		9	8	15
27	p14	fraction of C in leaf loss transferred to litter		0.48	0.1	0.7
28	p15	turnover rate of labile carbon	d^{-1}	0.09	1.00×10^{-4}	0.2
29	p16	fraction of labile transfers respired		0.15	0.01	0.5
30	p17	maximum CF value	$gC\, m^{-2}$	300	100	500
31	p18	leaf mass per area (lma)	$gC\, m^{-2}$	60	10	200
32	p19	threshold		100	80	120
33	p20	threshold		270	200	365

into the physical model and verified the final accuracy. After obtaining a parameter distribution with a resolution of 0.05° on the spatial scale, we estimated the LAI, GPP, ER, and NEE for the deciduous forests of the eastern United States.

3.3 Error evaluation

The evaluation in this paper involves three aspects: (1) verification of the accuracy of MASM when calibrating parameters; (2) verification of the feasibility of the XGBoost method in terms of predicting parameters; and (3) verification of the accuracy in spatial-scale and multi-product comparisons. We used Pearson's correlation coefficient (R), root mean square error (RMSE), average error (AE), and a comprehensive index called the distance between indices of simulation and observation (DISO) (Zhou et al., 2021; Hu et al., 2019) as statistical measures. AE can specify whether errors are overestimated or underestimated. RMSE is more sensitive to large errors. DISO used here is a combination of three widely used statistical metrics (R, normalized RMSE, and AE), aiming to identify the overall evaluation of each verification. When the DISO value is close to zero, the distance between the observed and simulated values is the closest, and the accuracy is the highest.

$$R = \frac{\sum_{i=1}^{n}(S_i - \overline{S})(O_i - \overline{O})}{\sqrt{\sum_{i=1}^{n}(S_i - \overline{S})^2}\sqrt{\sum_{i=1}^{n}(O_i - \overline{O})^2}} \tag{9}$$

$$AE = \frac{1}{n}\sum_{i=1}^{n}(S_i - O_i) \tag{10}$$

$$RMSE = \sqrt{\frac{1}{n}\sum_{i=1}^{n}(S_i - O_i)^2} \tag{11}$$

$$DISO = \sqrt{(R-1)^2 + \frac{AE^2}{\overline{O}} + \frac{RMSE^2}{\overline{O}}}, \tag{12}$$
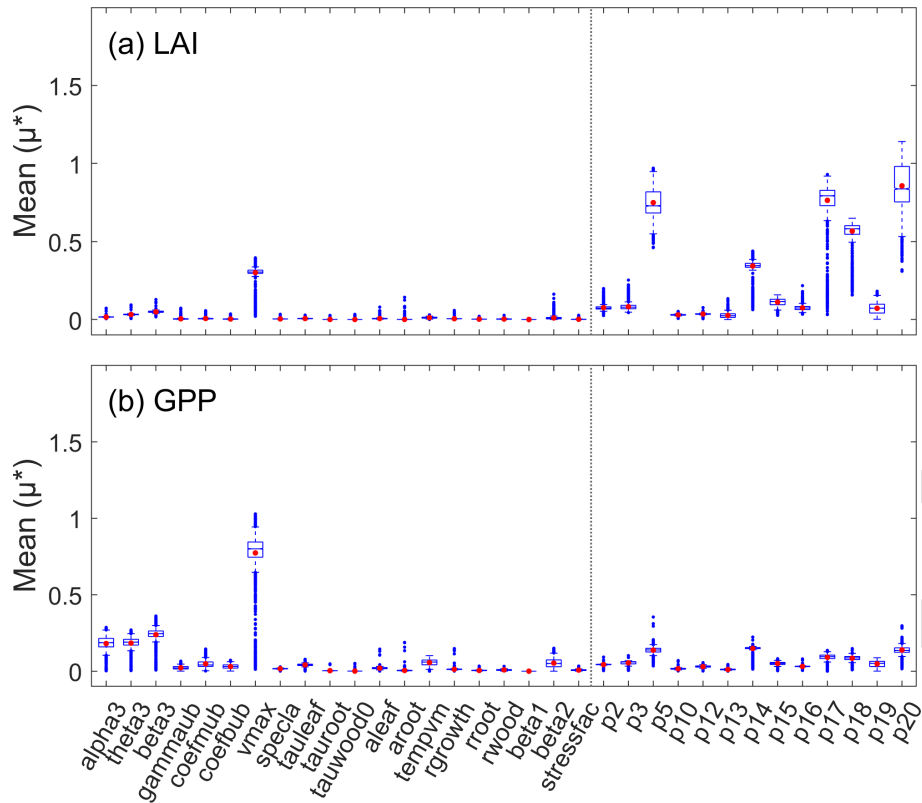
Figure 1. Sensitivity of **(a)** LAI and **(b)** GPP to all the parameters. The box chart shows the average and quartile of the Morris sensitivity index for all the samples. The red dots represent the mean, the blue midline means the median, the black bottom and top lines of the rectangle are the maximum and minimum values, and the blue dots denote the outliers.

where n represents the total number of pixels, S_i and O_i denote the simulated and observed variables at the ith pixel, and $\overline{S}$ and $\overline{O}$ are averaged values.

4 Results

4.1 Adaptive surrogate modeling performance of selected samples

4.1.1 Parameter behaviors

After parameter calibration of all samples, the posterior parameter distributions of the 10 sensitive parameters under the joint constraint of GLASS LAI and GPP were obtained by considering the last 100 000 values. Here, we only showed the posterior distributions of 10 representative pixels that were randomly selected (Fig. 2). Parameter behaviors showing an obvious unimodal pattern were considered as well-constrained, the ranges of which were within the previous definition. Most sensitive parameters (except alpha3, theta3, and beta3) exhibited a well-constrained distribution but with different degrees of concentration. GPP had weak constraints on alpha3, theta3, and beta3, mainly reflected in the scattered distributions and wide fluctuation ranges. With the Morris in-

dex shown in Fig. 1, we found that GPP seemed insensitive to small perturbations of these parameters. Comparatively, one significant limitation occurred with vmax, the maximum carboxylase capacity of Rubisco, which had a pronounced effect on plant photosynthesis.

The model structure also affected the limiting effect of observations on parameters. The relationship between LAI and its sensitive parameters was more direct without repeated transmission through complex processes. Thus, the posterior distributions of most samples were well constrained. Edge-hitting distribution appeared when the previous ranges of parameters were unsuitable for selected samples, showing that retrieved values were clustered near the highest or lowest bounds of the prior ranges (Fig. 2, 1-3, and 6-6). The rationality of the parameter prior range is not discussed in this paper, but edge-hitting distribution emphasized the importance of prior knowledge for optimization. The differences between samples were related to the spatial variation of parameter sensitivity, and the quality of the GLASS GPP and LAI products.

The posterior mean was chosen as the best estimate of each parameter. Thus, we obtained the histogram distribution of the optimal parameters for all samples (Fig. 3). The optimal values of each parameter among samples had notice-
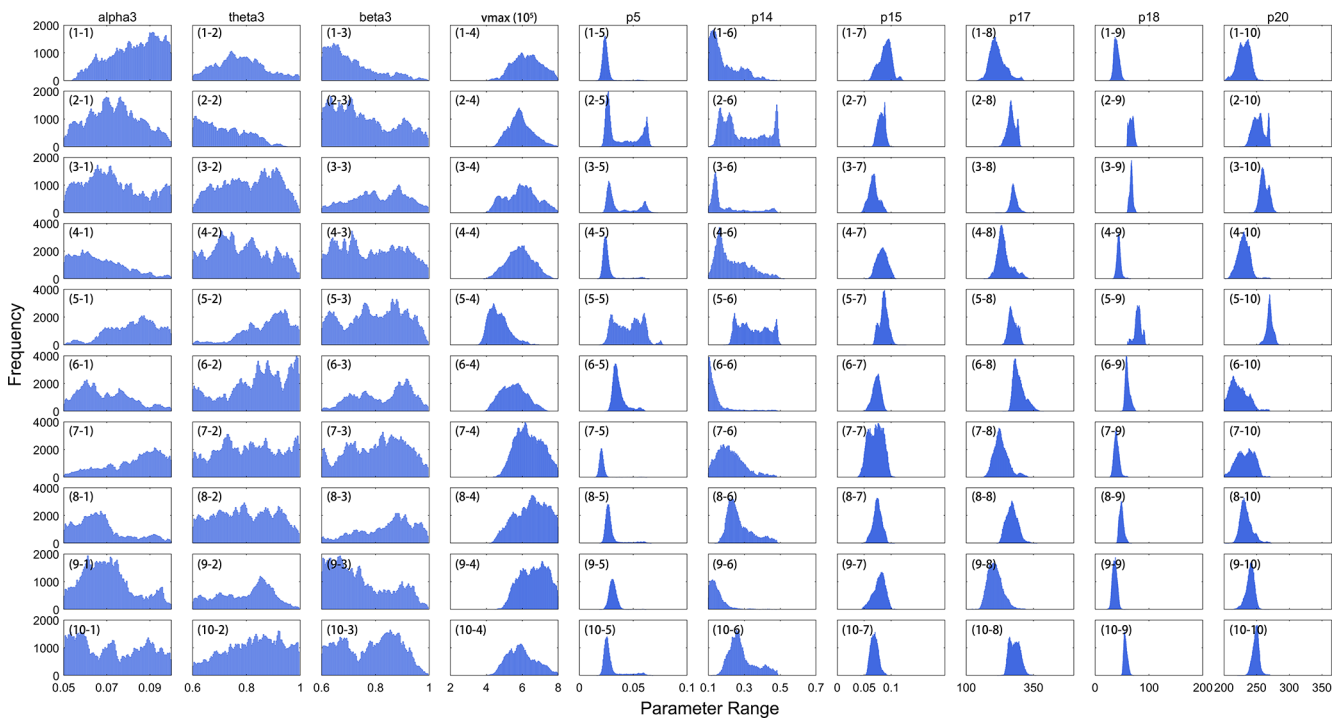
Figure 2. Posterior probability distribution of 10 representative samples.

able spatial variations that were significantly different from their default values. The Rubisco enzymes exhibited stronger carboxylase capacity, shown as higher vmax after calibration (Fig. 3d), and the leaf turnover rate (p5) also decreased by more than 30 % for most samples. For p14, the optimized value was less than half the default value, which indicated that the proportion of carbon in leaf loss transferred to litter was notably reduced. The results proved that using site-scale optimal parameters to define regional optimal schemes could not fully capture the discrepancy of ecophysical characteristics within a PFT, especially when a PFT type covers a large area.

4.1.2 Model improvement

With the constrained parameters resulting from the MASM optimization, we took the mean of each posterior distribution as the optimal value and re-entered it into the model to obtain the daily LAI and GPP simulations. Figure 4 shows the accuracy verification of LAI and GPP simulations against the GLASS products on the scale of every 8 d before and after parameter optimization.

We calculated the DISO value, a comprehensive indicator used for accuracy verification, for each sample. The histogram of DISO for all samples is illustrated in Fig. 4. For LAI, the DISO of more than 98 % pixels was less than 0.6, and the overall mean value was 0.33. For GPP, the DISO of more than 96 % of the pixels was less than 0.4, and the overall mean was 0.27. The calibrated IBIS model simulated LAI

well on an 8 d basis ($R^2 = 0.85$; RMSE = $0.664\,\mathrm{gC\,m^{-2}}$ per 8 d) in calibration years (2001–2009), while the accuracy of the validation years (2010–2018) slightly decreased. In comparison with GLASS GPP, the overall R^2 of the modeled GPP was 0.90, and the RMSE was close to $1.0\,\mathrm{gC\,m^{-2}}$ per 8 d. There was no significant difference in accuracy between the calibration and validation years, indicating that the calibrated parameters were stable over time. Our results demonstrated that the MASM approach was effective and efficient for providing approximately optimal parameters for a highly complex terrestrial biosphere model. Most optimization results showed good consistency with GLASS products.

4.2 Parameter distribution obtained by the XGBoost approach

4.2.1 Feature selection

The parameters calibrated in this study were divided into two categories: (1) parameters related to the photosynthesis process including alpha3, theta3, beta3, and vmax; and (2) parameters related to carbon conversion including p5, p14, p15, p17, p18, and p20 (Table 2). Considering the environmental heterogeneity of each pixel, we explored the relationship between these 10 parameters and local environmental characteristics from the aspects of climate, soil, location, and important surface variables (like LAI, GPP, and photosynthetically active radiation (PAR) that closely related to photosynthesis) (Table S2). The vapor pressure deficit (VPD), day
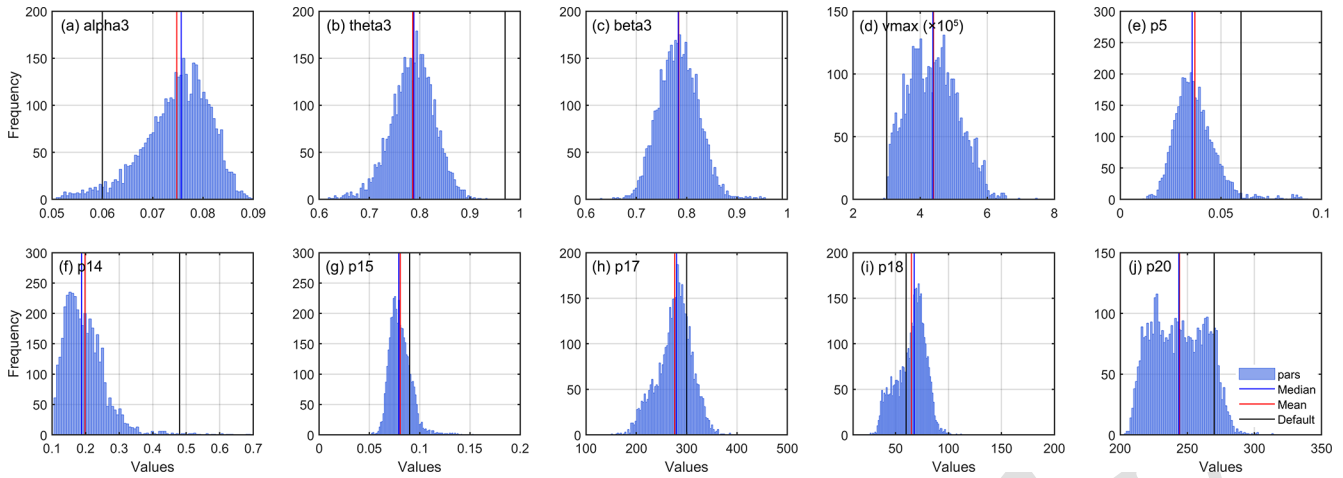
Figure 3. Histogram distribution of optimal parameters from all samples using the MASM optimization.
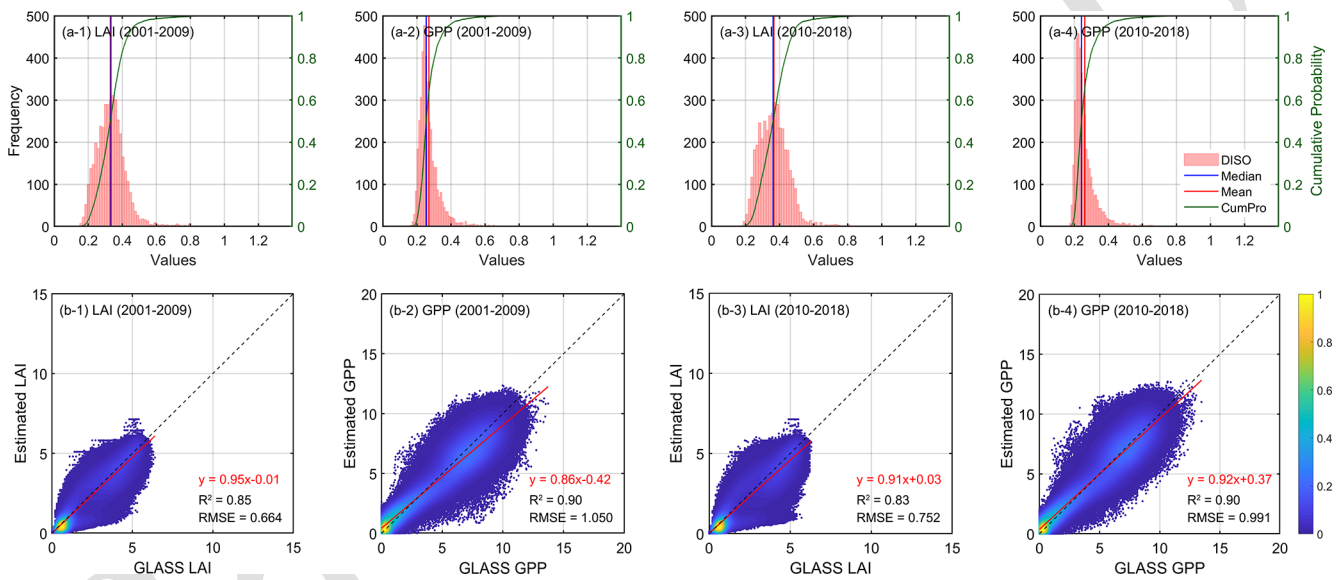
Figure 4. Validation of samples with optimal parameter schemes: **(a)** histogram statistics of DISO index for LAI **(a-1, a-2)** and GPP **(a-3, a-4)**, and scatter density plot of LAI **(b-1, b-2)** and GPP **(b-3, b-4)** against GLASS products on 8 d basis. Some samples that do not converge during the MASM process and show anomalous high errors are excluded. The calibration years are from 2001 to 2009, while the validation is from 2010 to 2018. "CumPro" in **(a)** represents the cumulative probability.

length, and shortwave radiation data (SRAD) were also considered as influence factors. VPD affects the rate and intensity of evapotranspiration. When plants close their stomata to adapt to high VPD, photosynthesis slows down and the growth rate slows down (Y. Li et al., 2018). Shortwave radiation provides the energy for photosynthesis; temperature and sunshine length in the growing season also affect the gas exchange characteristics of leaves (Rogers, 2014). We also added elevation information as areas with high altitudes are less affected by human activities and may have a higher carbon sequestration capacity compared with low-altitude areas.

4.2.2 XGBoost setting

We used the annual mean values of the selected features and the growth season statistics of temperature, VPD, SRAD, and PAR as the inputs of XGBoost modeling. We set 10 optimal parameters obtained by MASM as the target variables (i.e., the outputs of XGBoost). However, it was not guaranteed that posterior values obtained through the MASM approach were the best selection for each pixel due to observation (GLASS products) quality and algorithm uncertainty. Large errors indicated that calibrated parameters were not suitable for those samples, which would affect spatial prediction if they were included in training data for machine learning. In this paper,

the screening indexes were defined according to the DISO values of LAI and GPP. All the samples with DISO <0.35 (Fig. 4) were selected as the ML inputs, considering both the accuracy and sizes of the training samples. Finally, a total of 1930 samples were selected for spatial parameter prediction. We used 70 % of the selected samples to train the XGBoost model and the rest as an independent testing set.

4.2.3 XGBoost validation

Figure 5 shows the validation after running XGBoost methods. For parameters with strong effects (e.g., vmax, p18) on GPP and LAI, the fitting accuracy could reach more than 0.8, while parameters with lower sensitivity (like alpha3, theta3, beta3, p14, and p15) tended to have slightly lower accuracy. This is because, in the MASM optimization process, the optimal parameters were mainly constrained by LAI and GPP data, which also led to a more prominent order of LAI and GPP in feature importance ranking when the XGBoost model was trained.

When the parameters from the XGBoost simulation and MASM posterior distributions were used for the IBIS model, the estimated LAI and GPP showed high correlations with those of the GLASS products (2001–2018). For LAI, the correlation was above 0.6, while that of GPP was mostly above 0.8. Parameters obtained by XGBoost and MASM were highly consistent in capturing the degree of correlation with GLASS products. For the testing set, the estimated errors (RMSE and DISO) using XGBoost were slightly less correlated with the corresponding accuracy indexes of the MASM approach, but the range was similar. DISO was distributed below 0.5 of LAI, while GPP was distributed below 0.3. For the RMSE and DISO indexes, samples above the diagonal indicated results better estimated using MASM-optimized parameters, and those below the diagonal were better estimated by using parameters for the XGBoost simulation. The XGBoost performance was superior to that of MASM in terms of the final validation of parameters. For example, for testing LAI (Fig. 6c-3), 52 % of the pixels showed that the parameters obtained by XGBoost were more accurate, while the ratio reached 60 % for testing GPP (Fig. 6d-3). The possible explanation was that XGBoost used more environment variables related to the parameter; hence, the results may be more appropriate for each pixel. Moreover, the uncertainty of the MASM algorithm and the diversity of the posterior probability distribution model also affected the selection of the optimal parameters. In addition to better accuracy, another benefit of using the XGBoost method was that the calculation cost of parameter calibration was greatly reduced compared to surrogate modeling optimization.

4.2.4 Spatial parameter distribution

By combining the environmental characteristics, the optimal parameter distribution of each pixel was estimated for the en-

tire deciduous forest area (0.05°) in the eastern United States with the application of the trained XGBoost. Figure 7 shows the spatial distribution of each parameter. Vmax was higher in the central and northeastern parts of the deciduous forests, indicating that the Rubisco enzyme had a higher maximum carboxylase capacity in these regions. Parameters related to vegetation carbon turnover and allocation include p5, p14, and p15, which indicated a high turnover and allocation ratio in the western and northwestern areas. Leaf mass per area, shown as p18, was low in the northeast and about three times higher in parts of the south and southwest of the study region.

Compared with the original parameter ranges, the posterior distributions were significantly more concentrated (see "Pars_Hist" in Fig. 7). The overall ranges were greatly reduced, especially for theta3, beta3, p15, p17, and p18. There was a great difference in the distribution between optimal parameters and default values in the whole study area. For theta3 and beta3, the default values were outside the whole statistical range, which would induce a large error when using defaults to estimate carbon fluxes. For vmax, the optimal values were higher than the default values and had evident spatial heterogeneity. Vmax is a key source of uncertainty in current ecosystem models, and adopting a fixed value may give rise to large systematic error (Croft et al., 2017; Bonan et al., 2011; Liu et al., 2014; Walker et al., 2014). Rogers (2014) surveyed the derivation of vmax in earth system models and found a wide range of variation among vegetation types, and Bonan et al. (2011) showed that model uncertainty resulting from this parameter was comparable with that from the model structure.

4.3 Model improvement

### 4.3.1 Uncertainties in optimized LAI and GPP

Using the parameters estimated by XGBoost, we obtained the spatiotemporal distribution of optimized LAI and GPP. The estimated LAI and GPP before and after optimization were compared with those of the GLASS products. Figure 8 shows the frequency distribution of the accuracy indexes (R^2, RMSE, Bias, and DISO) of pixel-by-pixel validation in the deciduous forests from 2001 to 2018. The correlation coefficients of LAI and GPP before and after optimization showed little change. For LAI, the correlation of most pixels was above 0.6 (Fig. 8a-1), and for GPP, it was above 0.8 (Fig. 8b-1). However, the RMSE of the optimized parameters was reduced by 0.56 and 0.45 for LAI and GPP, respectively. We comprehensively evaluated the performance of both LAI and GPP with the DISO index. We found that for LAI, the DISO was less than 1 for 60 % of the pixels before optimization and was less than 0.3 for nearly 90 % of the pixels after optimization. Similarly, for GPP, the DISO decreased by 0.16 on average and the overall distribution became more concentrated.
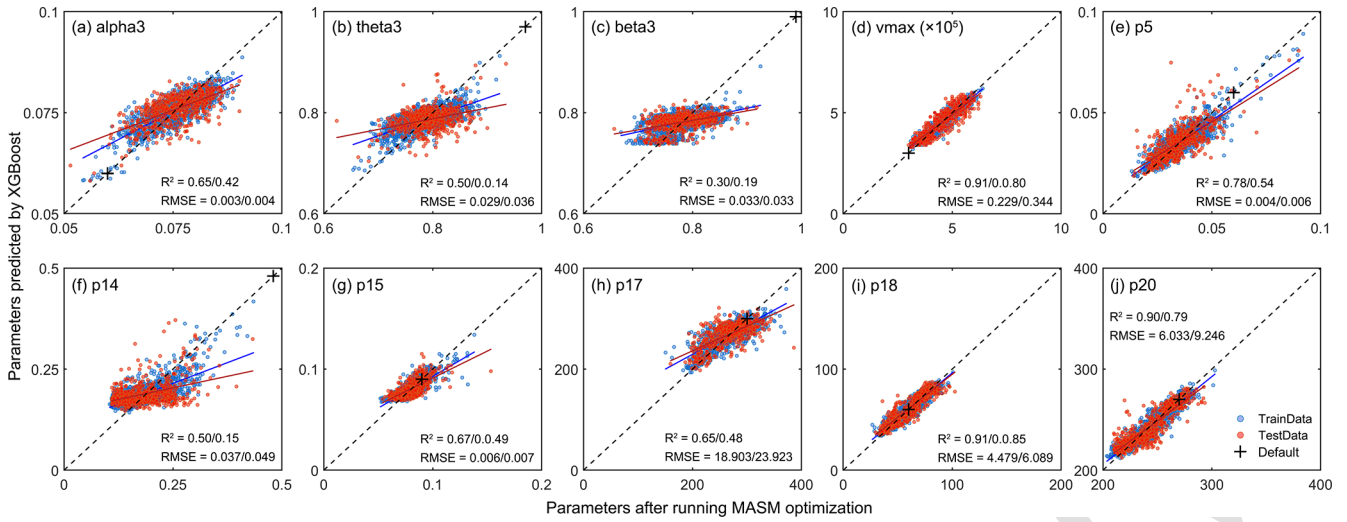
Figure 5. Scatter plots of the results of the XGBoost model. The *x* axis represents parameters after running MASM optimization and *y* axis means values obtained from XGBoost model. The means before and after the slash represent the accuracy indexes of the training set and testing sets, respectively. The blue dots represent the training set and red dots represent the testing set. The black cross indicates default values.
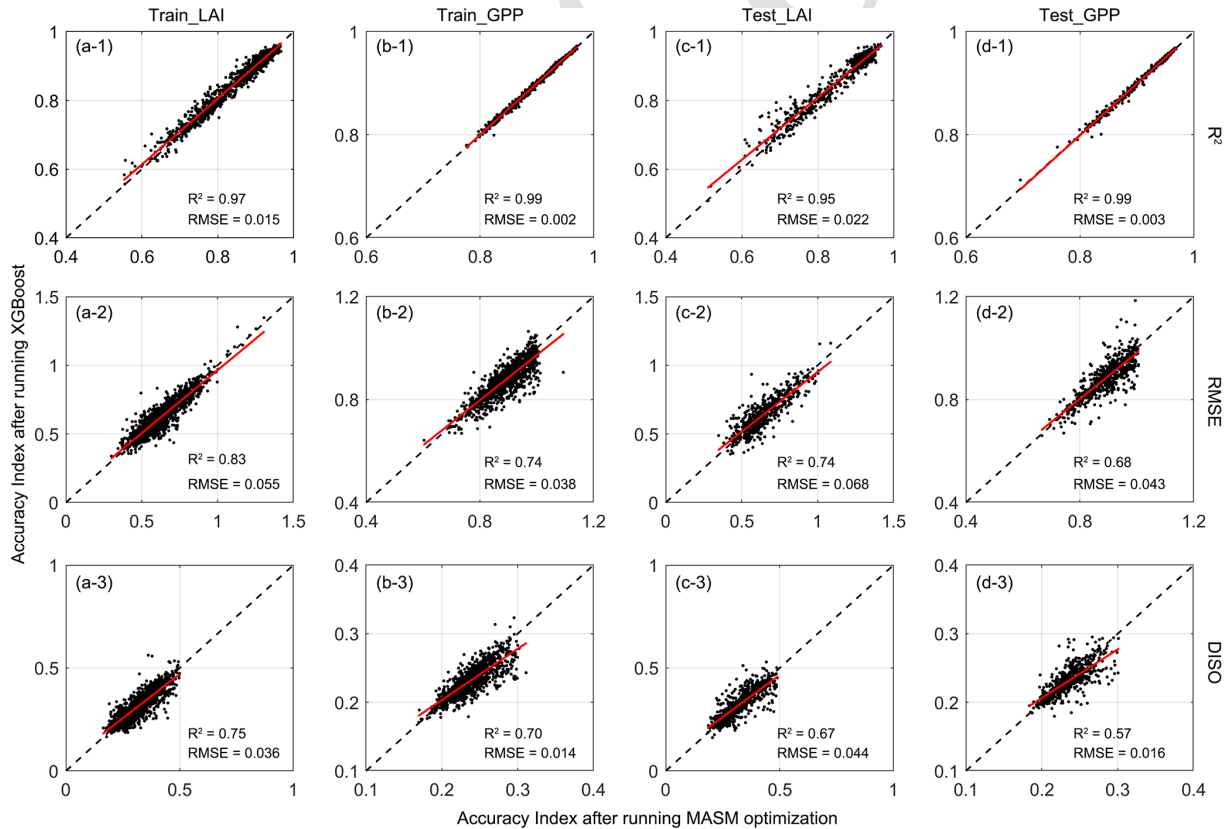
Figure 6. Accuracy indexes (R^2, RMSE, and DISO) validation between trained and predicted parameters in simulating LAI and GPP. The *x* axis represents the accuracy index using MASM posterior parameters; the *y* axis represents the accuracy index using estimated parameters from the trained XGBoost model.
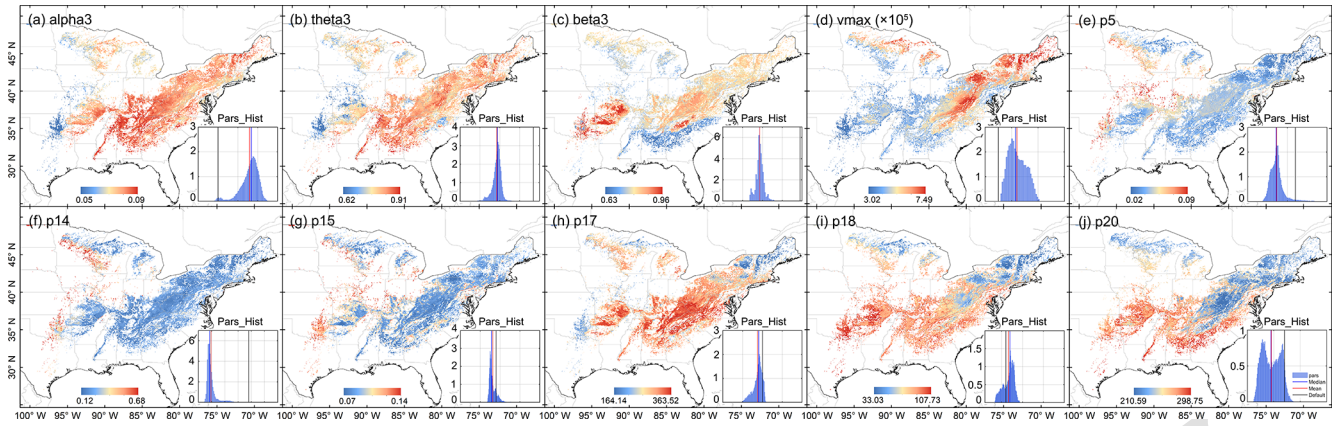
Figure 7. Spatial distribution of posterior parameter. The inset in the lower right corner of each plot represents the spatial distribution histogram of each parameter.
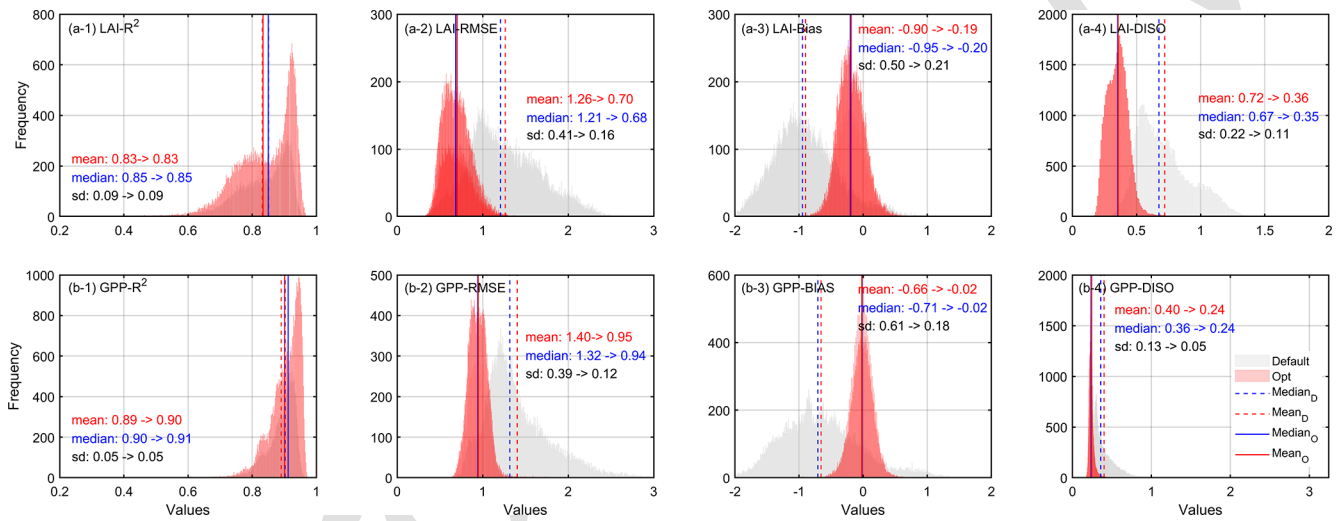
Figure 8. Histogram error statistics of LAI and GPP by running prior and posterior parameter schemes.

Figure 9 manifests the spatial distribution of the absolute error between estimated variables and GLASS products. The error distributions of the default parameters indicated that the error of LAI and GPP had similar spatial distributions. A high discrepancy of the previous model compared with GLASS mainly occurred in the middle and northwest parts of the study area. The absolute errors were dramatically improved after optimization. For LAI, the overall error was below $0.6\,\mathrm{m^2\,m^{-2}}$; for GPP, the errors in some central areas were between $0.6\,\mathrm{gC\,m^{-2}}$ per 8 d and $0.9\,\mathrm{gC\,m^{-2}}$ per 8 d, and they were below $0.6\,\mathrm{gC\,m^{-2}\,8d^{-1}}$ for the rest. The reduction of model errors was not consistent across pixels dominated by deciduous forests.

4.3.2 Site-level validation in carbon fluxes

Compared with the default estimates, our optimized fluxes had improved with RMSE reduced by 12 % for GPP, 20.38 % for ER and 1.57 % for NEE, while the correlation coefficients decreased slightly for GPP and NEE (Fig. S2). Using DISO as a comprehensive evaluation indicator, we verified the GPP before and after optimization at 14 flux sites, and also summarized the effect of parameter optimization on ER and NEE for every 8 d. When the GLASS GPP product was regarded as the "true value", the optimized model successfully estimated the magnitudes and temporal variations of GPP, and the DISO values of several sites improved by more than half throughout the whole year (e.g., US-Bar, US-LPH) (Fig. 10, gray bars). This is because the GLASS GPP product was used as the reference while calibrating the sensitive parameters. Considering the uncertainties of the GLASS product, we evaluated GPP, ER, and NEE using data from flux observation sites as a "true value". Collectively, the optimized model improved the flux estimates at most flux towers compared with those from the original model (DISO >0). We also evaluated the model performances in the growing sea-
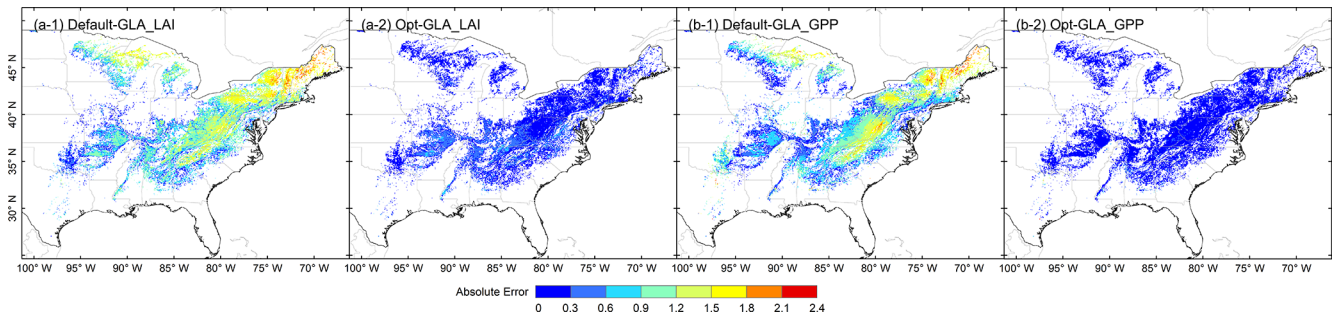
Figure 9. Spatial distribution of annual absolute error between model results and GLASS products from 2001 to 2018. **(a-1)** and **(a-2)** are the absolute difference of prior and posterior LAI, respectively; **(b-1)** and **(b-2)** are the absolute difference of prior and posterior GPP, respectively.

son and non-growing season, and found that GPP and NEE in the growing season were improved at most of the sites such as US-Ha1, US-UMB, US-Umd and US-WCr. However, for the non-growing season (NGS), the GPP accuracy decreased, and the corresponding NEE also showed greater inconsistency with the flux site NEE. Larger time-series differences during NGS between optimized and observed fluxes also existed at most sites compared to the default fluxes. The decrease of GPP accuracy is the main contributor to the larger errors of NEE estimates for most flux sites, while for US-Wi3, ER showed lower accuracy.

We calculated the DISO indicators between GLASS GPP and flux observations (DGLA) for the three periods (annual, growing season, and non-growing season) (see DGLA values shown in Fig. 10). The values of DISO in the non-growing season were significantly higher than those in GS, especially at the US-Bar, US-Wi1, and US-LPH sites, which indicated that GLASS GPP had a lower performance in the non-growing season for these 14 sites. This also explains why the difference between the optimized carbon fluxes and the observation was larger in the non-growing season. For US-Wi8, the GLASS GPP differed greatly from the observed data (with DISO of 1.12), and therefore the optimized results showed lower accuracy than those based on the default parameters. The timing of the peak GPP generally closely matched that of the flux tower GPP, although there was still significant underestimation for several sites (e.g., US-LPH, US-MMS, and US-Oho).

4.3.3 Impacts on simulated regional vegetation carbon fluxes

We used our optimized model to estimate GPP, ER, and NEE for each $0.05° × 0.05°$ pixel across the deciduous forests in the eastern United States from 2000 to 2019. The spatial patterns of the 20-year mean annual carbon fluxes are shown in Fig. 11. For the simulation based on the default parameters, the overall distribution of GPP gradually increased from high latitude to low latitude. A similar trend was also shown in ER; a weak carbon sink was observed for the whole re-

gion. The patterns changed obviously after parameter optimization. After the optimization, the Southeast of the US and in particular the areas along the Appalachian Mountains, an ecoregion of temperate broadleaf and mixed forests, had the highest GPP (~ 1500–$2000\,\mathrm{gC\,m^{-2}\,yr^{-1}}$); lower annual GPP was found in the West of the study region; ER generally exhibited similar patterns and was systematically lower than GPP estimates. For part of the western region, NEE was less than $200\,\mathrm{gC\,m^{-2}\,yr^{-1}}$, also in correspondence with areas characterized by low estimated GPP and ER. The spatial patterns of carbon fluxes with optimized parameters exhibited obvious spatial details and provided more reasonable spatial information.

Figure 12 showed the interannual variability in carbon fluxes (Fig. 12a) and percentages of variation after optimization for the whole year, the growing season, and non-growing season (Fig. 12b–c). The mean annual GPP, ER, and NEE over the deciduous forests in the eastern United States for the period from 2000 to 2019 were 5.79, 4.60, and $-1.19\,\mathrm{Pg\,yr^{-1}}$, respectively. The optimized GPP and ER were significantly higher than the defaults, and the capacity of carbon sequestration in deciduous forests also increased by more than half. We compared the impacts of the optimized model on different periods (annual, growing season, and non-growing season) and found that our estimates of GPP and ER were higher than previous estimates, of which the increase in the non-growing season was the most significant. For NEE, the capacity of deciduous forests to absorb carbon increased slightly in the growing season, while the estimates of carbon release decreased in the non-growing season, leading to an increase in carbon sequestration throughout the year.

5 Discussion

### 5.1 Algorithmic uncertainty

Our pixel-level calibration was divided into two parts. The first part used the MASM algorithm to calibrate each sample. We recorded the simulated CF of GPR model constructed in
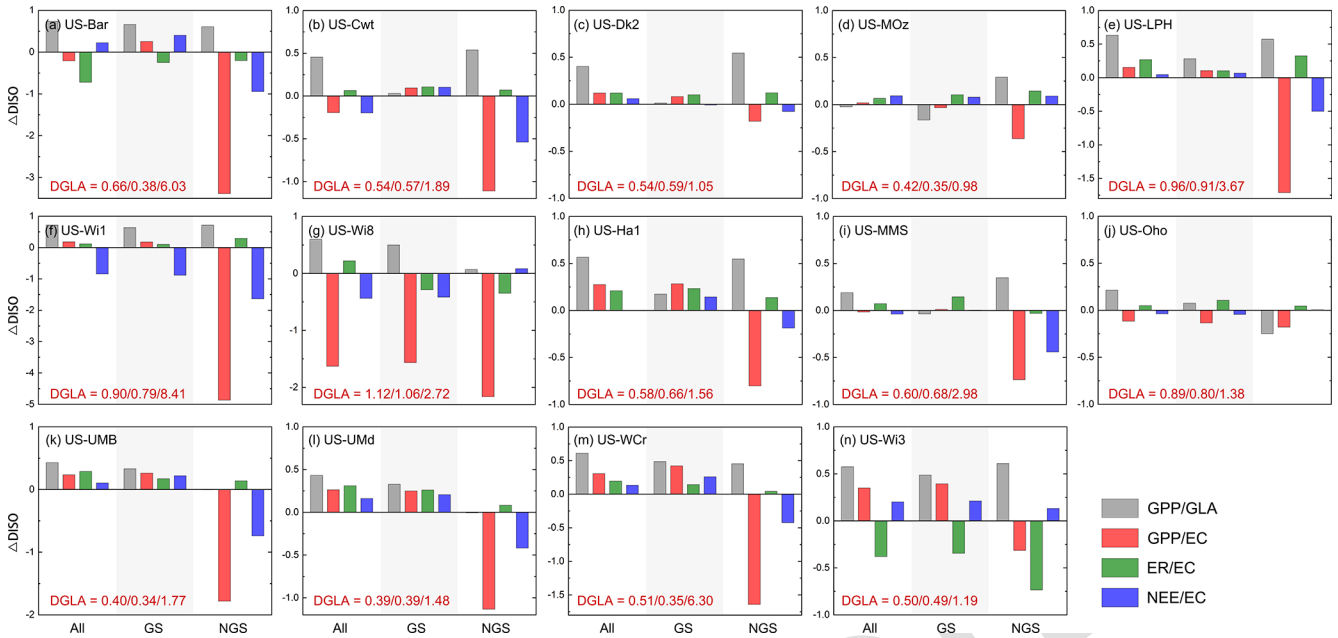
Figure 10. Optimized carbon fluxes performances for 14 flux sites throughout the whole year (All), growing season (GS, May to September), and non-growing season periods (NGS). The y axis means the changes between the DISO indexes before and after the optimization: $\Delta \text{DISO} = -(\text{DISO}_{\text{Opt}} - \text{DISO}_{\text{Def}})/\text{DISO}_{\text{Def}}$. Positive values represent improvement. The gray bars (GPP/GLA) represent the DISO index between the modeled GPP and the GLASS GPP products, while the red (GPP/EC), green (ER/EC), and blue (NEE/EC) bars mean the DISO index between the modeled fluxes (GPP, ER, and NEE) and the observed values at each flux site, respectively. EC represents the flux observations. The bottom left of each pattern shows the DISO index between the GLASS GPP product and the observations (DGLA) throughout three periods (All, GS and NGS).
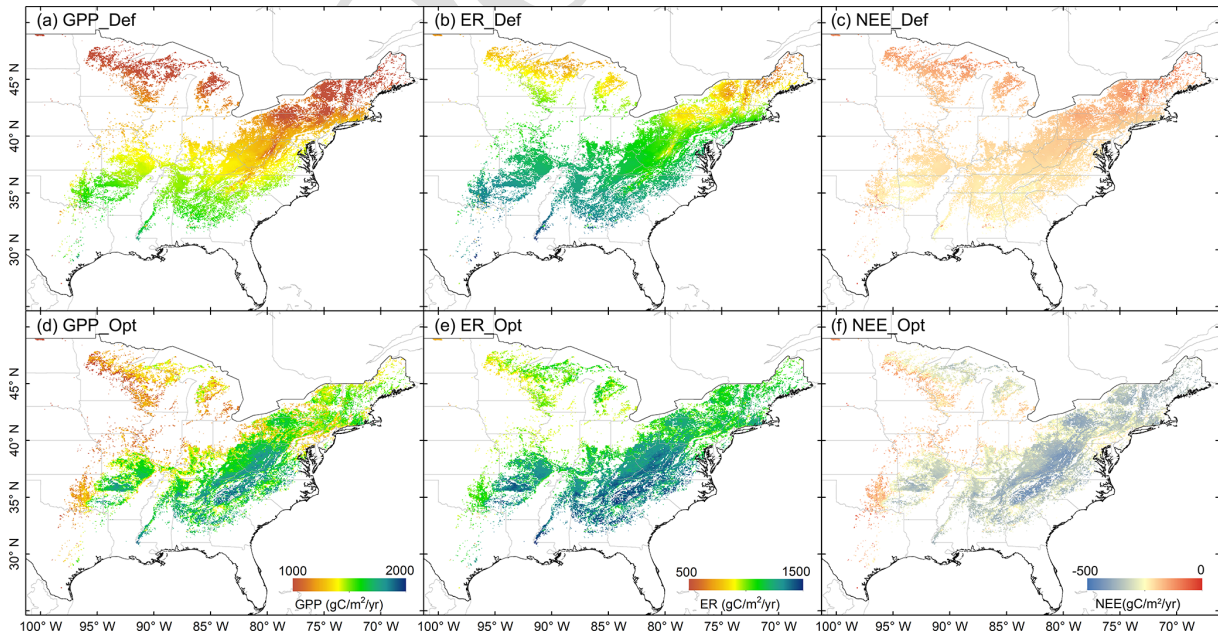
Figure 11. Regional patterns of mean annual carbon fluxes (GPP, NEE, and ER) for the years 2000–2019. Panels **(a)**–**(c)** show spatial distribution of each flux from the model with default parameters and **(d)**–**(f)** show distributions with optimized scheme.
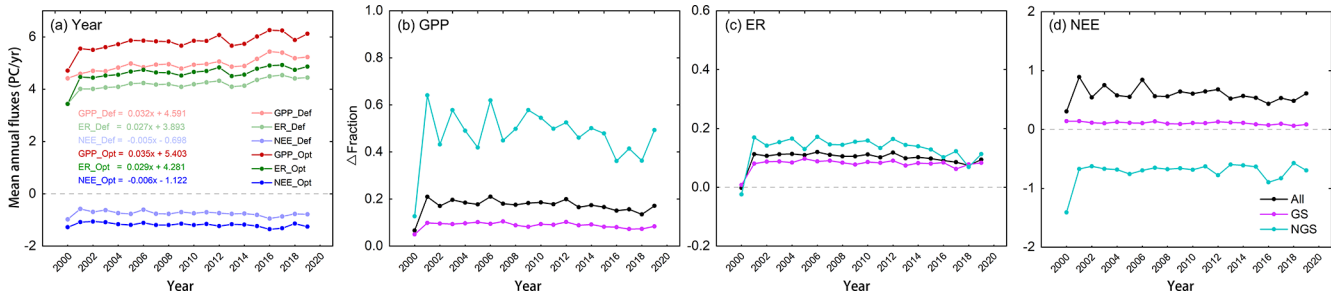
Figure 12. Temporal variations of each carbon flux (GPP, NEE, and ER) over the deciduous forests in the eastern US (2000–2019). **(a)** shows the interannual variation before and after parameter optimization. **(b)**–**(c)** represent the fraction changes after optimization, where positive fraction indicates an increase from the default fluxes and negative value indicates a decreasing impact.

each adaptive resampling and the simulated value of the real model, which was expressed by GPR_{RMSE} to measure the accuracy of the GPR model. We also calculated the average of the last 100 000 CFs after finishing the second iteration optimization, which was represented by CF_{mean}.

It was found that they were correlated and had unusually high values (Fig. S3). When the error of the GPR model was large (i.e., the GPR model cannot accurately represent the IBIS model), it was difficult to produce a smaller CF through iterative optimization. Therefore, the optimal parameter scheme for such samples would cause large errors when simulating LAI and GPP. From an algorithmic perspective, the number of iterations may have been insufficient during MCMC sampling. However, it should be noted that the increased number of iterations definitely increased the calculation cost. Two reasons could explain MASM uncertainty: (1) different samples may have had different sensitivity to parameters, and therefore we could not guarantee that the sensitive parameters of every sample were highly correlated with the model error; and (2) the prior range of parameters may have been inappropriate, failing to obtain a suitable combination. To ensure the accuracy of the input training set during the later training of the XGBoost model, sample pixels with excessive GPR_{RMSE} and CF_{mean} values were eliminated. In addition, most sample pixels converged to a stationary distribution with GR <1.2 in the second iteration optimization, while very few pixels that did not meet the convergence condition after 10 cycles were eliminated. We also performed quality control on samples when using XGBoost to simulate spatial optimal parameters to ensure the accuracy of input parameters.

5.2 Uncertainty of optimal parameters

It was found that the posterior distribution of the optimized parameters in each pixel had significant differences in distribution forms (single peak or multipeak), mean values, and fluctuations. The poorly constrained results meant that the model predictions were slightly sensitive while changing those parameters; for a multipeak distribution, there were

multiple combination schemes for this sample that met the requirement of minimum CF; and edge patterns representing posterior values were skewed to one side of the previous ranges, which reflected the defect of the model structures or the irrationality of the prior parameter ranges (Liu et al., 2015; Mäkelä et al., 2019). The uncertainty boundaries of these parameters were likely to be unrealistic and could lead to overconfidence in model predictions (Lu et al., 2017). The limiting effect of observations was strongly related to the sensitivity of observed variables to parameters, which indicated that the spatial variability of parameter sensitivity should also be considered in parameter optimization. The interaction between parameters should also be considered in parameter estimation (Fig. S4).

We provided an optimal parameter scheme for each pixel of the eastern United States and a more concentrated range of proposed parameters through the calibration that may be helpful for others to further find optimal parameters with high efficiency within this area. Although there had been many studies on parameter calibration, significant inconsistency still existed among the same parameters for different ecosystem models. This was mainly because the model and input data errors were compensated by parameter adjustment, and therefore it was difficult to ensure that the estimated parameters could be explained theoretically. When expanding the spatial domain of parameters, the limited understanding of the influences on each parameter also prevented us from estimating the actual values of these parameters. For example, previous studies found that vmax is closely related to leaf nitrogen content, and an increase of phosphorus content in leaves significantly improves the sensitivity of vmax to leaf nitrogen (Walker et al., 2014). Leaf and labile carbon turnover rates (p5, p15) were key factors determining the carbon sequestration capacity of terrestrial ecosystems. Wang et al. (2017) studied the biological and abiotic factors affecting forest carbon turnover time through quadrat observation and showed that multiple factors such as soil nutrients (e.g., carbon, nitrogen, and phosphorus), pH, and forest ages could not be ignored. It was also pointed out that the carbon turnover time could vary with time, which was not con-

sidered in this study. In addition, the calculation of LAI in DALEC was so simple that the sensitive parameters involved were correlated with LAI values. However, the calculation of GPP in IBIS involved many complex biochemical processes and factors, and thus the effect of GPP on parameters was not apparent. We could not guarantee that the parameters of each pixel were well-constrained in sample calibration. For samples with poor and edge-hitting constraints, if the simulated LAI and GPP showed good accuracy, we also took the optimal values as training samples for XGBoost, which could negatively impact model prediction.

5.3 The quality of optimized carbon fluxes

Generally, the previously estimated carbon fluxes matched the distribution of several key environmental variables (e.g., temperature, day length, radiation, specific humidity) more closely (Fig. S5), the trend of which was that the photosynthesis and respiration of deciduous forests gradually increased with the decrease of latitude. The information provided by climate conditions was reflected in the carbon flux simulation through the simulation of the model. As the physiological parameters used in each pixel were uniform values in the original model and only a single vegetation type was considered, the sources of spatial differences in carbon fluxes were mainly from the differences in driving data sets. The integration of GLASS products introduced the spatial distribution pattern information of the LAI and GPP products into the model by adjusting the distribution pattern of key parameters, which made the optimized spatial pattern distribution more reasonable. The optimized model with calibrated parameters can provide more accurate LAI and GPP information and the temporal and spatial distribution of both LAI and GPP were closer to those of the GLASS products. Although a decrease in the RMSE of the optimized fluxes performed a better validation, particularly around the period of peak fluxes, the results also indicated that when there is quite a distinction between GLASS and ground observation, it is difficult to successfully capture the variations of each flux site. For example, our results of most sites (e.g., US-Bar, US-WCr, and US-Wi3) showed that optimized NEE exhibited overestimation of net carbon uptake during the non-growing season. Overall, the accuracy of ER and NEE was not significantly improved based on the site-level validation (Fig. S2; Fig. 10). The reason for this may be that respiration is closely related to the size of carbon pools, while factors related to forest age and carbon pools are not considered in our current research. We will try to integrate forest age and biomass products to improve the key parameters of terrestrial carbon pools (such as allocation, turnover rate, and respiration rate) in the next exploration so that we can improve the simulation of respiration and vegetation carbon storage.

It is already known that the accuracy of spatial reference products (GLASS products in this paper) is the key factor affecting the accuracy of carbon fluxes during the model–data

fusion. The GLASS LAI and GPP products have been validated against globally available ground measurements and compared with several different simulations from other products. The results showed that GLASS products performed well in accuracy validation and spatial–temporal variations (Zheng et al., 2020; Ma and Liang, 2022). We also compared the accuracy differences between GLASS GPP product and several other GPP products (GPP derived from Breathing Earth System Simulator – BESS, GPP derived from the Vegetation Photosynthesis Model – VPM, GPP derived from the upscaling approaches based on machine learning methods – FLUXCOM, and MODIS) in our research region before regarding as a reference while optimizing parameters, and found that GLASS estimated GPP fairly well. The R^2 of GLASS is almost identical with that of other products; the RMSE of GLASS is slightly lower than that of BESS and comparable to that of VPM, FLUXCOM, and MODIS (Fig. S6). In fact, no matter which set of products is used, there will be certain errors in the product itself. The focus of this paper is to emphasize that the two-step optimization algorithm that we have developed can obtain the optimal parameter scheme pixel by pixel in space, and effectively reduce the time cost of parameter optimization. Compared with the default parameter scheme, the pixel-level optimization has significantly improved the LAI and GPP estimates. In the next experiment, we will try to use multiple sets of remote sensing products (e.g., BESS, VPM, FLUXCOM, MODIS for GPP), and use the triple-collocation method to give the spatial distribution of the error variance of the products, and take this error into account in the parameter optimization.

Multiple data streams and more relevant state variables should be applied as a way to mitigate the deviations from a single product or variable. We considered both LAI and GPP in the optimization but their contributions to the model improvement were not evaluated separately, which should be taken into account in future work. ML provides a convenient approach for integrating more spatial products with physical models, and we expect more explorations on developing a hybrid modeling framework to couple ML with physical models or explain and even compensate model errors due to lack of prior knowledge. Such a combination can increase the credibility of future carbon budget estimation and strengthen the rationality and interpretability of ML. In addition, we also put forward a demand for higher resolution and high-precision satellite products, which are necessary for model improvement and for carrying out benchmarking tests to comprehensively evaluate the performances of different models.

6 Conclusions

It was generally accepted that the model parameters had spatial heterogeneity, but calibrating a complex process-based model at the pixel level was not realistic, especially with an

increase in spatial resolution. This paper proposed a two-step framework for estimating optimal parameters at the pixel level. We randomly sampled the study area and used the GPR model as the surrogate model and then applied the MASM algorithm for iterative optimization to obtain the posterior distributions of samples. Next, we used XGBoost to describe the nonlinear relationship between optimal parameters and local climate, soil, and surface variables, and extend to the entire deciduous forests in the eastern United States. Our method provided an optimal parameter scheme for each pixel and confirmed that the discrepancy between GLASS products and predicted values was significantly reduced with the optimized parameters. The results showed that there was significant spatial variability of parameters within a vegetation type, and that using high-quality satellite products could efficiently calibrate the parameters of terrestrial biosphere models at the pixel level. Although we tested our approach only for deciduous forests of the eastern United States, it provided a feasible scheme for spatial calibration of other vegetation types, at higher resolutions and in larger areas.

References

Abatzoglou, J. T.: Development of gridded surface meteorological data for ecological applications and modelling, Int. J. Climatol., 33, 121–131, https://doi.org/10.1002/joc.3413, 2013.

Alton, P. B.: From site-level to global simulation: Reconciling carbon, water and energy fluxes over different spatial scales using a process-based ecophysiological land-surface model, Agr. Forest Meteorol., 176, 111–124, https://doi.org/10.1016/j.agrformet.2013.03.010, 2013.

Bacour, C., Peylin, P., MacBean, N., Rayner, P. J., Delage, F., Chevallier, F., Weiss, M., Demarty, J., Santaren, D., Baret, F., Berveiller, D., Dufrêne, E., and Prunet, P.: Joint assimilation of eddy covariance flux measurements and FAPAR products over temperate forests within a process-oriented biosphere model, J. Geophys. Res.-Biogeo., 120, 1839–1857, https://doi.org/10.1002/2015jg002966, 2015.

Barman, R., Jain, A. K., and Liang, M.: Climate-driven uncertainties in modeling terrestrial gross primary production: a site level to global-scale analysis, Glob. Change Biol., 20, 1394–1411, https://doi.org/10.1111/gcb.12474, 2014.

Bloom, A. A., Exbrayat, J.-F., van der Velde, I. R., Feng, L., and Williams, M.: The decadal state of the terrestrial carbon cycle: Global retrievals of terrestrial carbon allocation, pools, and residence times, P. Natl. Acad. Sci. USA, 113, 1285–1290, https://doi.org/10.1073/pnas.1515160113, 2016.

Bonan, G. B., Lawrence, P. J., Oleson, K. W., Levis, S., Jung, M., Reichstein, M., Lawrence, D. M., Swenson, S. C., Bonan, C., Lawrence, P. J., Oleson, K. W., Levis, S., Jung, M., Reichstein, M., Lawrence, D. M., and Swenson, S. C.: Improving canopy processes in the Community Land Model version 4 (CLM4) using global flux fields empirically inferred from FLUXNET data, J. Geophys. Res.-Biogeo., 116, G02014, https://doi.org/10.1029/2010JG001593, 2011.

Cao, X., Zhou, Z., Chen, X., Shao, W., and Wang, Z.: Improving leaf area index simulation of IBIS model and its effect on water carbon and energy – A case study in Changbai Mountain broadleaved forest of China, Ecol. Model., 303, 97–104, https://doi.org/10.1016/j.ecolmodel.2015.02.012, 2015.

Chaney, N. W., Herman, J. D., Ek, M. B., and Wood, E. F.: Deriving global parameter estimates for the Noah land surface model using

FLUXNET and machine learning, J. Geophys. Res.-Atmos., 121, 13–218, https://doi.org/10.1002/2016JD024821, 2016.

Chen, J. M., Ju, W., Ciais, P., Viovy, N., Liu, R., Liu, Y., and Lu, X.: Vegetation structural change since 1981 significantly enhanced the terrestrial carbon sink, Nat. Commun., 10, 4259, https://doi.org/10.1038/s41467-019-12257-8, 2019.

Chuter, A. M., Aston, P. J., Skeldon, A. C., and Roulstone, I.: A dynamical systems analysis of the data assimilation linked ecosystem carbon (DALEC) models, Chaos, 25, 036401, https://doi.org/10.1063/1.4897912, 2015.

Croft, H., Chen, J. M., Luo, X., Bartlett, P., Chen, B., and Staebler, R. M.: Leaf chlorophyll content as a proxy for leaf photosynthetic capacity, Global Change Biol., 23, 3513–3524, https://doi.org/10.1111/gcb.13599, 2017.

Cunha, A. P. M. A., Alvalá, R. C. S., Sampaio, G., Shimizu, M. H., and Costa, M. H.: Calibration and Validation of the Integrated Biosphere Simulator (IBIS) for a Brazilian Semiarid Region, J. Appl. Meteorol. Climatol., 52, 2753–2770, https://doi.org/10.1175/jamc-d-12-0190.1, 2013.

Dagon, K., Sanderson, B. M., Fisher, R. A., and Lawrence, D. M.: A machine learning approach to emulation and biophysical parameter estimation with the Community Land Model, version 5, Adv. Stat. Clim. Meteorol. Oceanogr., 6, 223–244, https://doi.org/10.5194/ascmo-6-223-2020, 2020.

Famiglietti, C. A., Smallman, T. L., Levine, P. A., Flack-Prain, S., Quetin, G. R., Meyer, V., Parazoo, N. C., Stettz, S. G., Yang, Y., Bonal, D., Bloom, A. A., Williams, M., and Konings, A. G.: Optimal model complexity for terrestrial carbon cycle prediction, Biogeosciences, 18, 2727–2754, https://doi.org/10.5194/bg-18-2727-2021, 2021.

Farquhar, G. D., von Caemmerer, S., and Berry, J. A.: A biochemical model of photosynthetic CO_2 assimilation in leaves of C_3 species, Planta, 149, 78–90, https://doi.org/10.1007/BF00386231, 1980.

Fer, I., Kelly, R., Moorcroft, P. R., Richardson, A. D., Cowdery, E. M., and Dietze, M. C.: Linking big models to big data: efficient ecosystem model calibration via Bayesian model emulation, Biogeosciences, 15, 5801–5830, https://doi.org/10.5194/bg-15-5801-2018, 2018.

Fernández-Martínez, M., Sardans, J., Chevallier, F., Ciais, P., Obersteiner, M., Vicca, S., Canadell, J. G., Bastos, A., Friedlingstein, P., Sitch, S., Piao, S. L., Janssens, I. A., and Peñuelas, J.: Global trends in carbon sinks and their relationships with CO_2 and temperature, Nat. Clim. Change, 9, 73–79, https://doi.org/10.1038/s41558-018-0367-7, 2018.

Foley, J. A., Prentice, I. C., Ramankutty, N., Levis, S., Pollard, D., Sitch, S., and Haxeltine, A.: An integrated biosphere model of land surface processes, terrestrial carbon balance, and vegetation dynamics, Global Biogeochem. Cy., 10, 603–628, https://doi.org/10.1029/96GB02692, 1996.

Forkel, M., Carvalhais, N., Schaphoff, S., v. Bloh, W., Migliavacca, M., Thurner, M., and Thonicke, K.: Identifying environmental controls on vegetation greenness phenology through model–data integration, Biogeosciences, 11, 7025–7050, https://doi.org/10.5194/bg-11-7025-2014, 2014.

Gong, W. and Duan, Q. Y.: An adaptive surrogate modelingbased sampling strategy for parameter optimization and distribution estimation (ASMO-PODE), Environ. Model. Softw., 95, 61–75, https://doi.org/10.1016/j.envsoft.2017.05.005, 2017.

Homer, C., Dewitz, J., Jin, S., Xian, G., Costello, C., Danielson, P., Gass, L., Funk, M., Wickham, J., Stehman, S., Auch, R., and Riitters, K.: Conterminous United States land cover change patterns 2001–2016 from the 2016 National Land Cover Database, ISPRS J. Photogramm. Remote Sens., 162, 184–199, https://doi.org/10.1016/j.isprsjprs.2020.02.019, 2020.

Hu, Z., Chen, X., Zhou, Q., Chen, D., and Li, J.: DISO: A rethink of Taylor diagram, Int. J. Climatol., 39, 2825–2832, https://doi.org/10.1002/joc.5972, 2019.

Keenan, T. F., Davidson, E., Moffat, A. M., Munger, W., and Richardson, A. D.: Using model-data fusion to interpret past trends, and quantify uncertainties in future projections, of terrestrial ecosystem carbon cycling, Glob. Change Biol., 18, 2555–2569, 10.1111/j.1365-2486.2012.02684.x, 2012.

Kucharik, C. J., Foley, J. A., Delire, C., Fisher, V. A., Coe, M. T., Lenters, J. D., Young-Molling, C., Ramankutty, N., Norman, J. M., and Gower, S. T.: Testing the performance of a dynamic global ecosystem model: water balance, carbon balance, and vegetation structure, Global Biogeochem. Cy., 14, 795–825, https://doi.org/10.1029/1999GB001138, 2000.

Kucharik, C. J., Barford, C. C., Maayar, M. E., Wofsy, S. C., Monson, R. K., and Baldocchi, D. D.: A multiyear evaluation of a Dynamic Global Vegetation Model at three AmeriFlux forest sites: Vegetation structure, phenology, soil temperature, and CO_2 and H_2O vapor exchange, Ecol. Model., 196, 1–31, https://doi.org/10.1016/j.ecolmodel.2005.11.031, 2006.

Kumar, S. V., Holmes, T. R., Bindlish, R., de Jeu, R., and Peters-Lidard, C.: Assimilation of vegetation optical depth retrievals from passive microwave radiometry, Hydrol. Earth Syst. Sci., 24, 3431–3450, https://doi.org/10.5194/hess-24-3431-2020, 2020.

Kuppel, S., Peylin, P., Maignan, F., Chevallier, F., Kiely, G., Montagnani, L., and Cescatti, A.: Model–data fusion across ecosystems: from multisite optimizations to global simulations, Geosci. Model Dev., 7, 2581–2597, https://doi.org/10.5194/gmd-7-2581-2014, 2014.

LDAS: NLDAS-2 Forcing Dataset, Land Data Assimilation Systems [data set], https://ldas.gsfc.nasa.gov/nldas/NLDAS2forcing.php (last access: 9 January 2021), 2016.

Li, J., Duan, Q., Wang, Y.-P., Gong, W., Gan, Y., and Wang, C.: Parameter optimization for carbon and water fluxes in two global land surface models based on surrogate modelling, Int. J. Climatol., 38, e1016–e1031, https://doi.org/10.1002/joc.5428, 2018.

Li, Y., Zhou, L., Wang, S., Chi, Y., and Chen, J.: Leaf Temperature and Vapour Pressure Deficit (VPD) Driving Stomatal Conductance and Biochemical Processes of Leaf Photosynthetic Rate in a Subtropical Evergreen Coniferous Plantation, Sustainability, 10, 4063, https://doi.org/10.3390/su10114063, 2018.

Liang, S., Cheng, J., Jia, K., Jiang, B., Liu, Q., Xiao, Z., Yao, Y., Yuan, W., Zhang, X., Zhao, X., and Zhou, J.: The Global Land Surface Satellite (GLASS) Product Suite, B. Am. Meteorol. Soc. 102, E323–E337, https://doi.org/10.1175/bams-d-18-0341.1, 2021.

Liu, D., Cai, W., Xia, J., Dong, W., Zhou, G., Chen, Y., Zhang, H., and Yuan, W.: Global validation of a process-based model on vegetation gross primary production using eddy covariance observations, PLoS One, 9, e110407, https://doi.org/10.1371/journal.pone.0110407, 2014.

Liu, M., He, H., Ren, X., Sun, X., Yu, G., Han, S., Wang, H., and Zhou, G.: The effects of constraining variables on

parameter optimization in carbon and water flux modeling over different forest ecosystems, Ecol. Model., 303, 30–41, https://doi.org/10.1016/j.ecolmodel.2015.01.027, 2015.

Liu, X., Liang, S., Li, B., Ma, H., and He, T.: Mapping 30 m Fractional Forest Cover over China's Three-North Region from Landsat-8 Data Using Ensemble Machine Learning Methods, Remote Sens., 13, 2592, https://doi.org/10.3390/rs13132592, 2021.

Lu, D., Ricciuto, D., Walker, A., Safta, C., and Munger, W.: Bayesian calibration of terrestrial ecosystem models: a study of advanced Markov chain Monte Carlo methods, Biogeosciences, 14, 4295–4314, https://doi.org/10.5194/bg-14-4295-2017, 2017.

Ma, H. and Liang, S. L.: Development of the GLASS 250-m Leaf Area Index Product (Version 6) from MODIS data using the bidirectional LSTM deep learning model, Remote Sens. Environ., 273, 112985, https://doi.org/10.1016/j.rse.2022.112985, 2022.

Ma, R., Xiao, J., Liang, S., Ma, H., He, T., Guo, D., Liu, X., and Lu, H.: Modified adaptive surrogate modeling (MASM) (v1.0), Zenodo [code], https://doi.org/10.5281/zenodo.6953354, 2022.

MacBean, N., Peylin, P., Chevallier, F., Scholze, M., and Schürmann, G.: Consistent assimilation of multiple data streams in a carbon cycle data assimilation system, Geosci. Model Dev., 9, 3569–3588, https://doi.org/10.5194/gmd-9-3569-2016, 2016.

Mäkelä, J., Knauer, J., Aurela, M., Black, A., Heimann, M., Kobayashi, H., Lohila, A., Mammarella, I., Margolis, H., Markkanen, T., Susiluoto, J., Thum, T., Viskari, T., Zaehle, S., and Aalto, T.: Parameter calibration and stomatal conductance formulation comparison for boreal forests with adaptive population importance sampler in the land surface model JSBACH, Geosci. Model Dev., 12, 4075–4098, https://doi.org/10.5194/gmd-12-4075-2019, 2019.

Morris, M. D.: Factorial Sampling Plans for Preliminary Computational Experiments, Technometrics, 33, 161–174, 1991.

NCEP: National Centers for Environmental Prediction (NCEP) North American Regional Reanalysis (NARR), in: Research Data Archive at the National Center for Atmospheric Research, Computational and Information Systems Laboratory, Boulder, CO [data set], https://psl.noaa.gov/data/gridded/data.narr.html (last access: 19 January 2021), 2005.

Owen, A. B.: Controlling Correlations in Latin Hypercube Samples, J. Am. Stat. Assoc., 89, 1517–1522, https://doi.org/10.1080/01621459.1994.10476891, 1994.

Pastorello, G., Trotta, C., and Canfora, E., et al.: The FLUXNET2015 dataset and the ONEFlux processing pipeline for eddy covariance data, Sci. Data, 7, 225, https://doi.org/10.1038/s41597-020-0534-3, 2020.

Peaucelle, M., Bacour, C., Ciais, P., Vuichard, N., Kuppel, S., Peñuelas, J., Marchesini, L. B., Blanken, P. D., Buchmann, N., Chen, J., Delpierre, N., Desai, A. R., Dufrene, E., Gianelle, D., Gimeno-Colera, C., Gruening, C., Helfter, C., Hörtnagl, L., Ibrom, A., Joffre, R., Kato, T., Kolb, T. E., Law, B., Lindroth, A., Mammarella, I., Merbold, L., Minerbi, S., Montagnani, L., Šigut, L., Sutton, M., Varlagin, A., Vesala, T., Wohlfahrt, G., Wolf, S., Yakir, D., and Viovy, N.: Covariations between plant functional traits emerge from constraining parameterization of a terrestrial biosphere model, Glob. Ecol. Biogeogr., 28, 1351–1365, https://doi.org/10.1111/geb.12937, 2019.

Piao, S., Wang, X., Wang, K., Li, X., Bastos, A., Canadell, J. G., Ciais, P., Friedlingstein, P., and Sitch, S.: Interannual variation of terrestrial carbon cycle: Issues and perspectives, Global Change Biol., 26, 300–318, https://doi.org/10.1111/gcb.14884, 2020.

Pilaš, I., Gašparović, M., Novkinić, A., and Klobučar, D.: Mapping of the Canopy Openings in Mixed Beech–Fir Forest at Sentinel-2 Subpixel Level Using UAV and Machine Learning Approach, Remote Sens., 12, 3925, https://doi.org/10.3390/rs12233925, 2020.

Raoult, N. M., Jupp, T. E., Cox, P. M., and Luke, C. M.: Land-surface parameter optimisation using data assimilation techniques: the adJULES system V1.0, Geosci. Model Dev., 9, 2833–2852, https://doi.org/10.5194/gmd-9-2833-2016, 2016.

Reichstein, M., Camps-Valls, G., Stevens, B., Jung, M., Denzler, J., Carvalhais, N., and Prabhat: Deep learning and process understanding for data-driven Earth system science, Nature, 566, 195–204, https://doi.org/10.1038/s41586-019-0912-1, 2019.

Rogers, A.: The use and misuse of $V_{c,max}$ in Earth System Models, Photosyn. Res., 119, 15–29, https://doi.org/10.1007/s11120-013-9818-1, 2014.

Gelman, A. and Rubin, D. B.: Inference from Iterative Simulation Using Multiple Sequences, Stat. Sci., 7, 457–472, https://doi.org/10.1214/ss/1177011136, 1992.

Ryu, Y., Jiang, C., Kobayashi, H., and Detto, M.: MODIS-derived global land products of shortwave radiation and diffuse and total photosynthetically active radiation at 5 km resolution from 2000, Remote Sens. Environ., 204, 812–825, https://doi.org/10.1016/j.rse.2017.09.021, 2018.

Safta, C., Ricciuto, D. M., Sargsyan, K., Debusschere, B., Najm, H. N., Williams, M., and Thornton, P. E.: Global sensitivity analysis, probabilistic calibration, and predictive assessment for the data assimilation linked ecosystem carbon model, Geosci. Model Dev., 8, 1899–1918, https://doi.org/10.5194/gmd-8-1899-2015, 2015.

Sawada, Y. and Koike, T.: Simultaneous estimation of both hydrological and ecological parameters in an ecohydrological model by assimilating microwave signal, J. Geophys. Res.-Atmos., 119, 8839–8857, https://doi.org/10.1002/2014JD021536, 2014.

Scholze, M., Kaminski, T., Knorr, W., Blessing, S., Vossbeck, M., Grant, J. P., and Scipal, K.: Simultaneous assimilation of SMOS soil moisture and atmospheric CO_2 in-situ observations to constrain the global terrestrial carbon cycle, Remote Sens. Environ., 180, 334–345, https://doi.org/10.1016/j.rse.2016.02.058, 2016.

Schürmann, G. J., Kaminski, T., Köstler, C., Carvalhais, N., Voßbeck, M., Kattge, J., Giering, R., Rödenbeck, C., Heimann, M., and Zaehle, S.: Constraining a land-surface model with multiple observations by application of the MPI-Carbon Cycle Data Assimilation System V1.0, Geosci. Model Dev., 9, 2999–3026, https://doi.org/10.5194/gmd-9-2999-2016, 2016.

Shangguan, W., Dai, Y., Duan, Q., Liu, B., and Yuan, H.: A global soil data set for earth system modeling, J. Adv. Model. Earth Syst., 6, 249–263, https://doi.org/10.1002/2013ms000293, 2014.

Tao, F., Zhou, Z., Huang, Y., Li, Q., Lu, X., Ma, S., Huang, X., Liang, Y., Hugelius, G., Jiang, L., Doughty, R., Ren, Z., and Luo, Y.: Deep Learning Optimizes Data-Driven Representation of Soil Organic Carbon in Earth System Model Over the Conterminous United States, Front. Big Data, 3, 17, https://doi.org/10.3389/fdata.2020.00017, 2020.

Thoning, K. W., Tans, P. P., and Komhyr, W. D.: Atmospheric carbon dioxide at Mauna Loa Observatory: 2. Analysis of the

NOAA GMCC data, 1974–1985, J. Geophys. Res.-Atmospheres, 94, 8549–8565, 1989.

Thornton, M. M., Shrestha, R., Thornton, P. E., Kao, S., Wei, Y., and Wilson, B. E.: Wilson: Daymet Version 4 Monthly Latency: Daily Surface Weather Data. ORNL DAAC, Oak Ridge, Tennessee, USA [dataset], https://doi.org/10.3334/ORNLDAAC/1904, 2021.

Varejão, C. G., Costa, M. H., and Camargos, C. C. S.: A multi-objective hierarchical calibration procedure for land surface/ecosystem models, Inverse Probl. Sci. Eng., 21, 357–386, https://doi.org/10.1080/17415977.2011.639453, 2013.

Walker, A. P., Beckerman, A. P., Gu, L., Kattge, J., Cernusak, L. A., Domingues, T. F., Scales, J. C., Wohlfahrt, G., Wullschleger, S. D., and Woodward, F. I.: The relationship of leaf photosynthetic traits – V_{cmax} and J_{max} – to leaf nitrogen, leaf phosphorus, and specific leaf area: a meta-analysis and modeling study, Ecol. Evol., 4, 3218–3235, https://doi.org/10.1002/ece3.1173, 2014.

Wang, C., Duan, Q., Gong, W., Ye, A., Di, Z., and Miao, C.: An evaluation of adaptive surrogate modeling based optimization with two benchmark problems, Environ. Modell. Softw., 60, 167–179, https://doi.org/10.1016/j.envsoft.2014.05.026, 2014.

Wang, J., Sun, J., Xia, J., He, N., Li, M., Niu, S., and Luo, Y.: Soil and vegetation carbon turnover times from tropical to boreal forests, Funct. Ecol., 32, 71–82, https://doi.org/10.1111/1365-2435.12914, 2017.

Wutzler, T. and Carvalhais, N.: Balancing multiple constraints in model-data integration: Weights and the parameter block approach, J. Geophys. Res.-Biogeo., 119, 2112–2129, https://doi.org/10.1002/2014jg002650, 2014.

Xiao, J., Davis, K. J., Urban, N. M., and Keller, K.: Uncertainty in model parameters and regional carbon fluxes: A model-data fusion approach, Agr. Forest Meteorol., 189–190, 175–186, https://doi.org/10.1016/j.agrformet.2014.01.022, 2014.

Xu, H., Zhang, T., Luo, Y., Huang, X., and Xue, W.: Parameter calibration in global soil carbon models using surrogate-based optimization, Geosci. Model Dev., 11, 3027–3044, https://doi.org/10.5194/gmd-11-3027-2018, 2018.

Yuan, W., Liang, S., Liu, S., Weng, E., Luo, Y., Hollinger, D., and Zhang, H.: Improving model parameter estimation using coupling relationships between vegetation production and ecosystem respiration, Ecol. Model., 240, 29–40, https://doi.org/10.1016/j.ecolmodel.2012.04.027, 2012.

Yuan, W., Liu, D., Dong, W., Liu, S., Zhou, G., Yu, G., Zhao, T., Feng, J., Ma, Z., Chen, J., Chen, Y., Chen, S., Han, S., Huang, J., Li, L., Liu, H., Liu, S., Ma, M., Wang, Y., Xia, J., Xu, W., Zhang, Q., Zhao, X., and Zhao, L.: Multiyear precipitation reduction strongly decreases carbon uptake over northern China, J. Geophys. Res.-Biogeo., 119, 881–896, https://doi.org/10.1002/2014jg002608, 2014.

Zhang, Q. R., Shi, L. S., Holzman, M., Ye, M., Wang, Y. K., Carmona, F., and Zha, Y. Y.: A dynamic data-driven method for dealing with model structural error in soil moisture data assimilation, Adv. Water Resour., 132, 103407, https://doi.org/10.1016/j.advwatres.2019.103407, 2019.

Zheng, Y., Shen, R., Wang, Y., Li, X., Liu, S., Liang, S., Chen, J. M., Ju, W., Zhang, L., and Yuan, W.: Improved estimate of global gross primary production for reproducing its long-term variation, 1982–2017, Earth Syst. Sci. Data, 12, 2725–2746, https://doi.org/10.5194/essd-12-2725-2020, 2020.

Zhong, L., Hu, L., and Zhou, H.: Deep learning based multi-temporal crop classification, Remote Sens. Environ., 221, 430–443, https://doi.org/10.1016/j.rse.2018.11.032, 2019.

Zhou, Q., Chen, D., Hu, Z., and Chen, X.: Decompositions of Taylor diagram and DISO performance criteria, Int. J. Climatol., 41, 5726–5732, https://doi.org/10.1002/joc.7149, 2021.

Zhou, Y., Williams, C. A., Lauvaux, T., Davis, K. J., Feng, S., Baker, I., Denning, S., and Wei, Y.: A multiyear gridded data ensemble of surface biogenic carbon fluxes for North America: evaluation and analysis of results, J. Geophys. Res.-Biogeo., 125, e2019JG005314, https://doi.org/10.1029/2019jg005314, 2020.

Zobitz, J. M., Moore, D. J. P., Quaife, T., Braswell, B. H., Bergeson, A., Anthony, J. A., and Monson, R. K.: Joint data assimilation of satellite reflectance and net ecosystem exchange data constrains ecosystem carbon fluxes at a high-elevation subalpine forest, Agr. Forest Meteorol., 195–196, 73–88, https://doi.org/10.1016/j.agrformet.2014.04.011, 2014.

Remarks from the typesetter

TS1 Please give an explanation of why this needs to be changed. We have to ask the handling editor for approval. Thanks.

TS2 Please give an explanation of why the equation needs to be changed. We have to ask the handling editor for approval. Please note that the remark has been left here for more clarity when reading the post-review adjustments file. You don't have to reply to this again.